

See discussions, stats, and author profiles for this publication at: <https://www.researchgate.net/publication/223569530>

# Uranyl adsorption and surface speciation at the imogolite–water interface: Self-consistent spectroscopic and surface complexation models

ARTICLE *in* GEOCHIMICA ET COSMOCHIMICA ACTA · JUNE 2006

Impact Factor: 4.33 · DOI: 10.1016/j.gca.2006.02.013

---

CITATIONS

70

---

READS

24

## 5 AUTHORS, INCLUDING:



**Yuji Arai**

University of Illinois, Urbana-Champaign

55 PUBLICATIONS 1,462 CITATIONS

SEE PROFILE



**John R. Bargar**

Stanford University

242 PUBLICATIONS 5,454 CITATIONS

SEE PROFILE



**James A. Davis**

Lawrence Berkeley National Laboratory

177 PUBLICATIONS 10,230 CITATIONS

SEE PROFILE

# Uranyl adsorption and surface speciation at the imogolite–water interface: Self-consistent spectroscopic and surface complexation models

Yuji Arai <sup>a,b,\*</sup>, M. McBeath <sup>a</sup>, J.R. Bargar <sup>c</sup>, J. Joye <sup>a</sup>, J.A. Davis <sup>a</sup>

<sup>a</sup> U.S. Geological Survey, Water Resource Division, 345 Middlefield Road MS 465, Menlo Park, CA 94025, USA

<sup>b</sup> University of Delaware, Department of Plant and Soil Sciences, Newark, DE 19717, USA

<sup>c</sup> Stanford Synchrotron Radiation Laboratory, P.O. Box 4349, Stanford, CA 94309, USA

Received 25 August 2005; accepted in revised form 20 February 2006

## Abstract

Macro- and molecular-scale knowledge of uranyl (U(VI)) partitioning reactions with soil/sediment mineral components is important in predicting U(VI) transport processes in the vadose zone and aquifers. In this study, U(VI) reactivity and surface speciation on a poorly crystalline aluminosilicate mineral, synthetic imogolite, were investigated using batch adsorption experiments, X-ray absorption spectroscopy (XAS), and surface complexation modeling. U(VI) uptake on imogolite surfaces was greatest at pH ~7–8 ( $I = 0.1$  M NaNO<sub>3</sub> solution, suspension density = 0.4 g/L [ $U(VI)_i$ ] = 0.01–30  $\mu$ M, equilibration with air). Uranyl uptake decreased with increasing sodium nitrate concentration in the range from 0.02 to 0.5 M. XAS analyses show that two U(VI) inner-sphere (bidentate mononuclear coordination on outer-wall aluminol groups) and one outer-sphere surface species are present on the imogolite surface, and the distribution of the surface species is pH dependent. At pH 8.8, bis-carbonato inner-sphere and tris-carbonato outer-sphere surface species are present. At pH 7, bis- and non-carbonato inner-sphere surface species co-exist, and the fraction of bis-carbonato species increases slightly with increasing  $I$  (0.1–0.5 M). At pH 5.3, U(VI) non-carbonato bidentate mononuclear surface species predominate (69%). A triple layer surface complexation model was developed with surface species that are consistent with the XAS analyses and macroscopic adsorption data. The proton stoichiometry of surface reactions was determined from both the pH dependence of U(VI) adsorption data in pH regions of surface species predominance and from bond-valence calculations. The bis-carbonato species required a distribution of surface charge between the surface and  $\beta$  charge planes in order to be consistent with both the spectroscopic and macroscopic adsorption data. This research indicates that U(VI)-carbonato ternary species on poorly crystalline aluminosilicate mineral surfaces may be important in controlling U(VI) mobility in low-temperature geochemical environments over a wide pH range (~5–9), even at the partial pressure of carbon dioxide of ambient air ( $p_{CO_2} = 10^{-3.45}$  atm).

© 2006 Elsevier Inc. All rights reserved.

## 1. Introduction

As a result of nuclear power plant and uranium mining operations, and nuclear weapons production, uranium (U) has been recognized as one of the most widespread radionuclide contaminants in soils and groundwater in the U.S. (Riley et al., 1992). In particular, at several U.S. Department of Energy sites (e.g., Hanford, Washington, Oak Ridge, Tennessee, and Savannah River, South Carolina), U plumes have been identified in the vadose and/or

saturated zones of the subsurface, and precise knowledge in predicting the fate and transport of U is greatly needed to protect and improve ground- and surface-water quality. In oxic environments, U is typically present in the hexavalent oxidation state, and adsorption of the uranyl oxocation ( $U(VI)O_2^{2+}$ ) on soil mineral surfaces is presumed to retard U(VI) mobility in subsurface environments (Davis et al., 2004).

Many researchers have investigated U(VI) adsorption on variable charge soil mineral surfaces. In the presence of carbonate anions, U(VI) retention generally maximizes at near neutral pH on aluminosilicate minerals (Borovec, 1981; Ames et al., 1983; McKinley et al., 1995; Payne

\* Corresponding author. Fax: +1 650 329 4327.

E-mail address: [yarai@usgs.gov](mailto:yarai@usgs.gov) (Y. Arai).

et al., 1998) and metal oxides (Maya, 1982; Ho and Miller, 1985; Hsi and Langmuir, 1985; Payne and Waite, 1991; Lieser et al., 1992; Waite et al., 1994; Duff and Amrhein, 1996). Several in situ spectroscopic techniques such as X-ray absorption, Raman, and luminescence spectroscopies have been widely used to elucidate the structure of U(VI) surface species at the mineral–water interface, and the results show that U(VI) surface species vary depending on the type of adsorbent and reaction conditions. Whereas the formation of inner-sphere bidentate binuclear complexes has been consistently reported on silica and  $\gamma$ -aluminum oxide surfaces (Glinka et al., 1995; Sylwester et al., 2000), two different U(VI) bonding mechanisms (i.e., ion exchange and chemisorption) as a function of pH and U(VI) loading levels have been suggested on smectite surfaces (Dent et al., 1992; Chisholm-Brause et al., 1994, 2004; Morris et al., 1994; Sylwester et al., 2000; Hennig et al., 2002). Iron oxides (i.e., hydrous ferric oxyhydroxide, lepidocrocite, and goethite) also serve as sinks for U(VI) by forming predominantly bidentate surface species (Manceau et al., 1992; Waite et al., 1994; Moyes et al., 2000; Dodge et al., 2002; Walter et al., 2003). More importantly, U(VI) in air-equilibrated hematite systems is known to form U(VI)-carbonate ternary complexes (Bargar et al., 1999, 2000). Recent grazing-incidence X-ray absorption spectroscopic studies indicated the formation of inner-sphere bidentate and outer-sphere complexes on rutile ( $\text{TiO}_2$ ) (110) and (001) planes, and inner-sphere surface species on  $\alpha$ - $\text{Al}_2\text{O}_3$  (1102) and (110) surfaces and  $\alpha$ - $\text{Fe}_2\text{O}_3$  (1102) surfaces (Den Auwer et al., 2003; Denecke et al., 2003; Catalano et al., 2005).

Although many of these studies have been concerned with U(VI) coordination environments at the surfaces of crystalline aluminosilicate minerals and metal oxides, there is a lack of knowledge of U(VI) reactivity and surface speciation on poorly crystalline aluminosilicate minerals, such as allophane and imogolite, that are important transient phases in soil weathering processes. Allophane and imogolite are commonly present in andisols and spodosols (Violante and Tait, 1979; Mckeague and Kodama, 1981; Farmer and Fraser, 1982; Dahlgren and Walker, 1993). Although the occurrence of these minerals is commonly reported in soils with accumulated volcanic ash, they have been also identified in pumice deposits, stream sediments, coatings of primary particles, and soils derived from igneous and sedimentary rock sandstones in different geographic regions (Violante and Tait, 1979; Jongmans et al., 1995; Harsh et al., 2002). Several researchers have demonstrated that poorly crystalline aluminosilicate minerals strongly retain various anions (i.e., phosphate and chloride) and cations (e.g., Al, Cd, Pb, and Cu) over a wide pH range in low-temperature geochemical environments (Theng et al., 1982; Clark and McBride, 1984; Wada, 1987; Harsh et al., 1992; Denaix et al., 1999), suggesting a possible important role in controlling the reactivity of anionic/cationic U(VI) aqueous species, such as  $\text{UO}_2^{2+}$  and  $\text{UO}_2(\text{CO}_3)_3^{4-}$  in soil solutions and groundwater. Further-

more, a recent study by Allard and co-workers have indicated that Al-rich poorly crystalline aluminosilicate gels from oxidative weathering of a U deposit in France retained a substantial amount of U(VI), indicating the important role of poorly crystalline aluminosilicate minerals as U(VI) sinks (Allard et al., 1999).

In this study, the high surface area, poorly crystalline aluminosilicate mineral, imogolite,  $\text{HOSiO}_3\text{Al}_2(\text{OH})_3$ , was chosen as a model adsorbent. U(VI) reactivity and surface speciation were examined as a function of pH and ionic strength, using batch adsorption experiments, X-ray absorption fine structure spectroscopic analyses, and surface complexation modeling. Typically, the selection of surface species for surface complexation models has been based on aqueous speciation models or chemical intuition; rarely has the choice of surface species been made based on spectroscopic evidence. In the modeling approach used here, spectroscopic identification of surface species was used to constrain the selection of surface species in model development and to ensure consistency between the model and spectroscopic results. Agreement between macroscopic U(VI) adsorption data and model calculations was attained by optimization of surface stability constants and charge distribution of species within the context of the triple layer modeling approach of Sverjensky (2005).

## 2. Materials and methods

### 2.1. Materials

Imogolite was synthesized according to the method described by Farmer et al. (1983).  $\text{Al}(\text{ClO}_4)_3 \cdot 9\text{H}_2\text{O}$  (0.1 M) stock solution was slowly added to 2 mM tetraethylorthosilicate solution to make a 4 L solution containing  $[\text{Al}]_{\text{total}} = 1.25 \text{ mM}$  and  $[\text{Si}]_{\text{total}} = 1.55 \text{ mM}$ . pH was adjusted to 5 with 1 M NaOH, and then the solution was immediately acidified to achieve final concentrations of nitric acid and acetic acid of 1 and 2 mM, respectively. The suspension was refluxed at 95–100 °C for 5 days. Gelatinous precipitates were flocculated by increasing the ionic strength to 0.5 M with added  $\text{NaNO}_3$ . The solids were concentrated by centrifugation and then washed with deionized water until the specific conductivity was reduced to less than 0.78 dS/m. Physicochemical properties of synthetic imogolite were confirmed by transmission electron microscopy (TEM) and diffuse reflectance Fourier transform infrared (DR-FTIR) spectroscopy. Transmission electron microscopy micrographs revealed distinctive tubular structure and FTIR spectra were similar to spectra of natural imogolite reported by Wada et al. (1979). The Brunauer–Emmett–Teller (BET) surface area of the dry imogolite was 166  $\text{m}^2/\text{g}$ . Ammonium oxalate digestion indicated a Al/Si ratio of  $2.10 \pm 0.14$ . The point of zero charge (PZC) was estimated at about 7.5 from a salt titration method; this intermediate value is expected since the surface consists of both aluminol external- and silanol inner-tubular sites.

The result agrees reasonably with the PZC values of natural imogolite of 7.4–9 determined by other investigators (Horikawa, 1975; Karube et al., 1992).

## 2.2. Uranyl adsorption experiments

U(VI) adsorption on synthetic imogolite (0.4 g/L suspended in 0.1 M NaNO<sub>3</sub> solution) was studied as a function of U(VI) concentration (total U(VI) concentrations of 0.01, 1, and 30 µM, abbreviated as  $U_{\text{tot}}$ ) and pH (3–10). A U(VI) stock solution with a concentration of 0.01 M at pH ~3 was prepared from isotopically depleted UO<sub>2</sub>(NO<sub>3</sub>)<sub>2</sub> · 6H<sub>2</sub>O reagent (Johnson-Matthey) and spiked with a <sup>233</sup>U(VI) tracer. Imogolite suspensions (0.42–0.48 g/L) were prepared in 50 ml polypropylene centrifuge tubes containing 0.1 M NaNO<sub>3</sub> solution. Sufficient amounts of 10 mM NaHCO<sub>3</sub> solution were added to achieve the desired bicarbonate concentration in equilibrium with the partial pressure of carbon dioxide gas in air ( $p_{\text{CO}_2} = 10^{-3.45}$  atm) at specified experimental pH values. After 24 h of equilibration with humidified air, a sufficient quantity of the UO<sub>2</sub>(NO<sub>3</sub>)<sub>2</sub> · 6H<sub>2</sub>O stock solution was added to the imogolite suspensions to assure  $U_{\text{tot}} = 0.01$ , 1, or 30 µM and a final suspension density of 0.4 g/L. The samples were reacted for 24 h on an end-over-end shaker operating at 12 rpm. The final pH was measured in the quiescent suspension and then the suspension was centrifuged at 20,190g for 10 min. The supernatant was filtered through 0.2 µm nylon filters (Pall Gelman, An Arbor, MI), and then acidified with 0.1 M HNO<sub>3</sub>. Three milliliters of supernatant was added to 15 ml of scintillation cocktail (Ecolite) and the activity of <sup>233</sup>U tracer was measured with a liquid scintillation counter (Beckman LS6500, multi-purpose scintillation counter). Adsorption experiments with 1 µM U(VI) were also studied at different electrolyte concentrations (i.e., 0.02 and 0.5 M NaNO<sub>3</sub> solutions).

## 2.3. Speciation calculations

All speciation and surface complexation modeling calculations were completed with the equilibrium speciation program, FITEQL 4.0, (Herbelin and Westall, 1999) and the uranium thermodynamic data given in Guillaumont et al. (2003). Table 1 lists the aqueous thermodynamic data used in the calculations. The Davies equation was used for activity correction (aqueous species only). Relative errors of 1% in the concentrations of surface sites, total U(VI), and adsorbed U(VI), and relative errors of 5% in log[H<sup>+</sup>] and log[H<sub>2</sub>CO<sub>3</sub>] were used as FITEQL input values.

## 2.4. Extended X-ray absorption fine structure spectroscopic measurements

U(VI) surface speciation on the imogolite surface (suspension density 0.3 g/L) was studied as a function of pH

Table 1  
Formation constants for aqueous species

Reaction	log β* ( <i>I</i> = 0) <sup>a</sup>
UO <sub>2</sub> <sup>2+</sup> + H <sub>2</sub> O ⇌ UO <sub>2</sub> OH <sup>+</sup> + H <sup>+</sup>	−5.25
UO <sub>2</sub> <sup>2+</sup> + 2H <sub>2</sub> O ⇌ UO <sub>2</sub> (OH) <sub>2,aq</sub> + 2H <sup>+</sup>	−12.15
UO <sub>2</sub> <sup>2+</sup> + 3H <sub>2</sub> O ⇌ UO <sub>2</sub> (OH) <sub>3</sub> <sup>−</sup> + 3H <sup>+</sup>	−20.25
UO <sub>2</sub> <sup>2+</sup> + 4H <sub>2</sub> O ⇌ UO <sub>2</sub> (OH) <sub>4</sub> <sup>2−</sup> + 4H <sup>+</sup>	−32.4
2UO <sub>2</sub> <sup>2+</sup> + H <sub>2</sub> O ⇌ (UO <sub>2</sub> ) <sub>2</sub> OH <sup>3+</sup> + H <sup>+</sup>	−2.70
2UO <sub>2</sub> <sup>2+</sup> + 2H <sub>2</sub> O ⇌ (UO <sub>2</sub> ) <sub>2</sub> (OH) <sub>2</sub> <sup>2+</sup> + 2H <sup>+</sup>	−5.62
3UO <sub>2</sub> <sup>2+</sup> + 4H <sub>2</sub> O ⇌ (UO <sub>2</sub> ) <sub>3</sub> (OH) <sub>4</sub> <sup>2+</sup> + 4H <sup>+</sup>	−11.90
3UO <sub>2</sub> <sup>2+</sup> + 5H <sub>2</sub> O ⇌ (UO <sub>2</sub> ) <sub>3</sub> (OH) <sub>5</sub> <sup>+</sup> + 5H <sup>+</sup>	−15.55
3UO <sub>2</sub> <sup>2+</sup> + 7H <sub>2</sub> O ⇌ (UO <sub>2</sub> ) <sub>3</sub> (OH) <sub>7</sub> <sup>−</sup> + 7H <sup>+</sup>	−32.2
4UO <sub>2</sub> <sup>2+</sup> + 7H <sub>2</sub> O ⇌ (UO <sub>2</sub> ) <sub>4</sub> (OH) <sub>7</sub> <sup>+</sup> + 7H <sup>+</sup>	−21.9
UO <sub>2</sub> <sup>2+</sup> + CO <sub>3</sub> <sup>2−</sup> ⇌ UO <sub>2</sub> CO <sub>3,aq</sub>	9.94
UO <sub>2</sub> <sup>2+</sup> + 2CO <sub>3</sub> <sup>2−</sup> ⇌ UO <sub>2</sub> (CO <sub>3</sub> ) <sub>2</sub> <sup>2−</sup>	16.61
UO <sub>2</sub> <sup>2+</sup> + 3CO <sub>3</sub> <sup>2−</sup> ⇌ UO <sub>2</sub> (CO <sub>3</sub> ) <sub>3</sub> <sup>4−</sup>	21.84
2UO <sub>2</sub> <sup>2+</sup> + CO <sub>3</sub> <sup>2−</sup> + 3H <sub>2</sub> O ⇌ (UO <sub>2</sub> ) <sub>2</sub> CO <sub>3</sub> (OH) <sub>3</sub> <sup>−</sup> + 3H <sup>+</sup>	−0.855
UO <sub>2</sub> <sup>2+</sup> + NO <sub>3</sub> <sup>−</sup> ⇌ UO <sub>2</sub> NO <sub>3</sub> <sup>+</sup>	0.3
UO <sub>2</sub> <sup>2+</sup> + Si(OH) <sub>4,aq</sub> ⇌ UO <sub>2</sub> SiO(OH) <sub>3</sub> <sup>+</sup> + H <sup>+</sup>	−1.84
H <sub>2</sub> CO <sub>3</sub> ⇌ H <sup>+</sup> + HCO <sub>3</sub> <sup>−</sup>	−6.35
H <sub>2</sub> CO <sub>3</sub> ⇌ 2H <sup>+</sup> + CO <sub>3</sub> <sup>2−</sup>	−16.68
Na + HCO <sub>3</sub> <sup>−</sup> ⇌ NaHCO <sub>3</sub> <sup>0</sup>	0.16 <sup>b</sup>
Na + CO <sub>3</sub> <sup>2−</sup> ⇌ NaCO <sub>3</sub> <sup>−</sup>	0.55 <sup>b</sup>

<sup>a</sup> All U(VI) values from Guillaumont et al. (2003).

<sup>b</sup> Values from Nakayama (1971).

(5.3, 7, and 8.8), U(VI) concentration ( $U_{\text{tot}}$  of 6 and 30 µM), and ionic strength ( $I = 0.1$  and 0.5 M NaNO<sub>3</sub>) with the partial pressure of carbon dioxide gas in air (see Table 2 for specific reaction conditions). Using aqueous speciation calculations, the final aqueous conditions were calculated to be undersaturated with respect to amorphous uranyl hydroxide UO<sub>2</sub>(OH)<sub>2</sub> (s) for all samples, but slightly supersaturated with respect to metaschoepite (UO<sub>3</sub> · 2H<sub>2</sub>O) for the pH 5.3 samples (Table 2). However, neither metaschoepite nor any other U(VI) precipitate was observed in any of the samples, as indicated by the results of our XAS analyses (see Section 3.2), and this result can be explained by kinetic limitations in the precipitation of crystalline U(VI) oxide or hydroxide hydrates. It has been shown that the first precipitate to appear under these conditions is typically amorphous uranyl hydroxide, which has a greater solubility than metaschoepite (Allard et al., 1999; Bargar et al., 2000).

All samples were prepared in 500 ml batch systems using the methods described above. The imogolite paste samples were recovered via centrifugation for 10 min at 20,190g. Dissolved U(VI) concentrations in the supernatant were analyzed using kinetic phosphorescence analysis (KPA, Chemchek Instruments). To minimize the entrained solution from well-hydrated imogolite, centrifugation was repeated twice with each sample. The samples were loaded in 3 mm Teflon sample holders, which were then sealed with Mylar/polycarbonate windows. The samples were wrapped with moist tissues and kept at ≈3–5 °C prior to XAS data collection. Room temperature U L<sub>III</sub> edge (17,166 eV) fluorescence spectra were collected within 36 h of sample preparation at the Stanford Synchrotron Radiation Laboratory (SSRL) beamline 4.3 (Si(220) dou-

Table 2

Total dissolved Al and Si ( $\mu\text{M}$ ) concentrations observed under different XAS reaction conditions (i.e.,  $[\text{NaNO}_3]$ ,  $[\text{U(VI)}]_T$ , and final pH) in  $p_{\text{CO}_2} = 10^{-3.45}$  atm

Final XAS sample conditions	Saturation index					
	am. $(\text{UO}_2)(\text{OH})_2(\text{H}_2\text{O})(\text{s})$			Metaschoepite, $\text{UO}_3 \cdot 2\text{H}_2\text{O}$		
$[\text{NaNO}_3]$ (M)	0.1	0.5	0.1	0.5	0.1	0.5
$p\text{H } 5.3$ , $[\text{U(VI)}]_T = 30 \mu\text{M}$						
$[\text{Al}]_T$ ( $\mu\text{M}$ )	4.3	B.D.	−1.10	−1.02	0.09	0.17
$[\text{Si}]_{\text{IT}}$ ( $\mu\text{M}$ )	6.7	17				
$p\text{H } 7$ , $[\text{U(VI)}]_T = 6 \mu\text{M}$						
$[\text{Al}]_T$ ( $\mu\text{M}$ )	0.7	B.D.	−2.47	−2.52	−1.28	−1.33
$[\text{Si}]_{\text{IT}}$ ( $\mu\text{M}$ )	5.7	2.7				
$p\text{H } 8.8$ , $[\text{U(VI)}]_T = 30 \mu\text{M}$						
$[\text{Al}]_T$ ( $\mu\text{M}$ )	B.D.	0.7	−4.79	−4.93	−3.60	−3.74
$[\text{Si}]_T$ ( $\mu\text{M}$ )	9.3	18				

SD for  $[\text{Al}]$  and  $[\text{Si}]$  ( $\mu\text{M}$ ) is  $\pm 0.2$ . B.D., below detection.

Saturation index values for am.  $(\text{UO}_2)(\text{OH})_2(\text{H}_2\text{O})(\text{s})$  ( $\log K = -22.00$ , Allard et al., 1984) and metaschoepite,  $(\text{UO}_3 \cdot 2\text{H}_2\text{O})$  ( $\log K = -23.19$ , Guillaumont et al., 2003) were estimated using  $[\text{U(VI)}]_T$ , pH, and ionic strength.

ble crystal monochromator) using a Xe-gas filled Lytle detector or a Canberra 13-element Ge detector array equipped with a Sr  $3 \mu\text{m}$  x filter. The storage ring was operated at 3 GeV energy with a current of 80–100 mA. Uranium or yttrium reference foil was used to calibrate at the U  $L_{\text{III}}$ - or Y K-edge absorption edge energy positions (17,166 and 17,038 eV, respectively) every 12 h.

The program FEFF 6 (Rehr et al., 1992) was used to estimate backscattering phases and amplitude functions of single scattering (SS)  $\text{U}-\text{O}_{\text{ax}}$ ,  $\text{U}-\text{O}_{\text{eq}}$ ,  $\text{U}-\text{C}$ ,  $\text{U}-\text{Si}$ , and transdioxo uranium multiple scattering paths (MS), which were derived from structural refinement data for anderssonite ( $\text{Na}_2\text{CaUO}_2(\text{CO}_3)_3 \cdot 5.33\text{H}_2\text{O}$ ) (Mereiter, 1986) and soddyite ( $(\text{UO}_2)_2(\text{SiO}_4)(\text{H}_2\text{O})_2$ ) (Belokoneva et al., 1979). A  $\text{U}-\text{Al}$  SS path was obtained from the structural refinement data of phurallumite ( $\text{Al}_2(\text{OH})_2(\text{PO}_4)_2(\text{UO}_2)_3(\text{OH})_4 \cdot 10\text{H}_2\text{O}$ ) (Piret et al., 1979). XAS data reduction and analyses were performed using the IFEFFIT engine-based interface, SixPACK (Webb, 2005).  $k^3$ -weighted Fourier transformed XAS spectra were fit in R-space over the range of 0–4.5 Å.

In the fit, CN and R for three transdioxo uranium MS paths (1,  $\text{U}=\text{O}_{\text{ax}}=\text{U}=\text{O}_{\text{ax}2}$ ; 2,  $\text{U}=\text{O}_{\text{ax}}=\text{O}_{\text{ax}2}$ ; and 3,  $\text{U}=\text{O}_{\text{ax}}=\text{U}=\text{O}_{\text{ax}}$ ) were calculated based on the fit derived values for axial shells (Hudson et al., 1996) CN, R, and  $\sigma^2$  of three transdioxo MS paths were fixed to 2,  $2 \times R_{\text{Oax}}$ , and  $2 \times \sigma_{\text{Oax}}^2$ , respectively.  $\Delta E_0$  was allowed to float and linked to all shells during the fit. To reduce the number of degrees of freedom, the Best Integer Fit method was used to constrain the coordination number 2 and 6 for  $\text{U}-\text{O}_{\text{ax}}$  and  $\text{O}_{\text{eq}}$  shells, respectively. To account for the changes in amplitude of two  $\text{U}-\text{O}_{\text{dist}}$  MS paths (3 and 4 legged) as a function of an angle ( $\beta$ ) of  $\text{U}-\text{O}_{\text{eq}}-\text{C}$  (Fig. 1), MS contributions of distal oxygen ( $\text{O}_{\text{dist}}$ ) atoms of carbonate

ions (1,  $\text{U}-\text{O}_{\text{dist}}$  ss; 2,  $\text{U}-\text{C}-\text{O}_{\text{dist}}$  (3-legged MS); and 3,  $\text{U}-\text{C}-\text{O}_{\text{dist}}$  (4-legged MS)) were included in the fit with a  $\text{U}-\text{O}_{\text{dist}}$  SS path. MS intensity as a function of the  $\beta$  angle ( $140^\circ$ – $180^\circ$ ) was calculated using FEFF702. The results are shown in Figs. 2a and b.

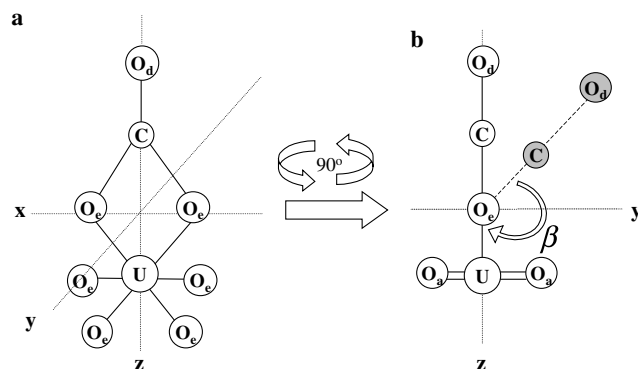


Fig. 1. Schematic figures of mono-carbonate U(VI) complexes on an  $x$ - $z$  plane (a) and a  $y$ - $z$  plane (b).  $\text{O}_{\text{ax}}$ , axial oxygen;  $\text{O}_{\text{d}}$ , distal oxygen;  $\text{O}_{\text{e}}$ , equatorial oxygen. Two axial oxygen atoms are omitted in (a). Four equatorial oxygen atoms are omitted in (b). A bending  $\text{U}-\text{O}_{\text{e}}-\text{C}$  angle is defined as  $\beta$ .

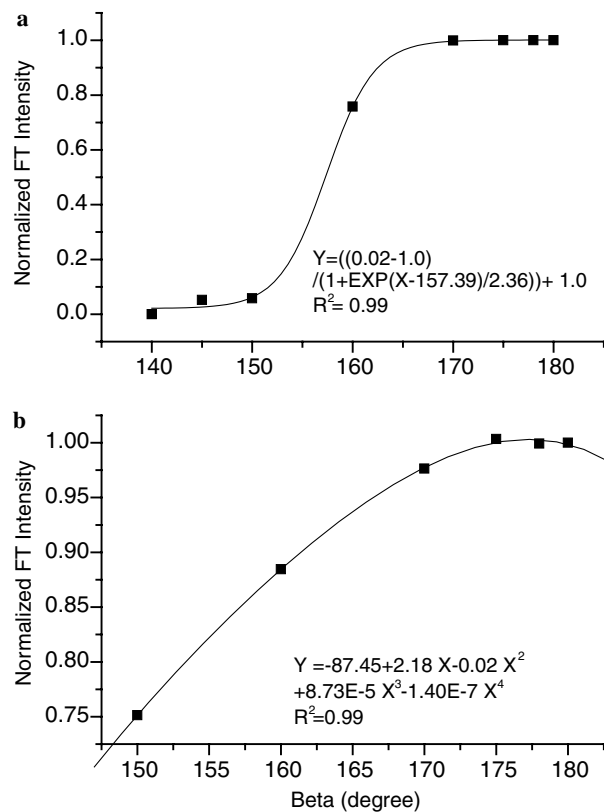


Fig. 2. Estimated amplitude factors (FT intensity) as a function of a  $\text{U}-\text{O}_{\text{eq}}-\text{C}$  bending angle ( $\beta = 140^\circ$ – $180^\circ$ ) for  $\text{U}-\text{C}-\text{O}_{\text{dist}}$  [(a) 4-legged and (b) 3-legged MS paths]. The non-linear relations for the 3-legged and 4-legged paths are shown in (a) and (b), respectively.



As described in Section 3.2, a maximum of four putative surface species (non-carbonato, mono-carbonato and bis-carbonato inner-sphere, and tris-carbonato outer-sphere surface species) were considered in the fit. Amplitude reduction factors for U–C and O<sub>dist</sub> shells were assumed to originate from four different fractions ( $F$ ) of U surface species (i.e., non-carbonato ( $F_{\text{non}}$ ), mono-carbonato ( $F_{\text{mono}}$ ), and bis-carbonato inner-sphere ( $F_{\text{bis}}$ ), and tris-carbonato outer-sphere surface species ( $F_{\text{tris}}$ )). Based on the assumption, we set the “total fraction ( $F$ ) = 1” as a summation of all fractions of surface species (i.e.,  $1 = F_{\text{non}} + F_{\text{mono}} + F_{\text{bis}} + F_{\text{tris}}$ ). The fractions for each mono- and bis-carbonato species (i.e., U–C SS, and U–O<sub>dist</sub> SS) were defined as “ $F_{\text{mono}} * S_o^2 * 1$ ” and “ $S_o^2 * F_{\text{bis}} * 2$ ,” respectively. For the tris-carbonato outer-sphere surface species, “ $S_o^2 * F_{\text{tris}} * 3$ ” was used only for defining the U–C SS and U–O<sub>dist</sub> SS paths. Based on the preliminary fit, we found a U–Al interatomic distance ( $\sim 3.3$  Å) corresponding to inner-sphere uranium bidentate *mononuclear* coordination with the aluminum octahedral structure (i.e., one Al atom is coordinated). Therefore, we used “ $S_o^2 * 1 * F_{\text{non}}$ ,” “ $S_o^2 * 1 * F_{\text{mono}}$ ,” and “ $S_o^2 * 1 * F_{\text{bis}}$ ” for the U–Al path for non-, mono-, and bis-carbonato inner-sphere surface species, respectively. For the amplitude functions of 3-legged and 4-legged U–O<sub>dist</sub> MS paths, previously derived non-linear functions (Figs. 2a and b) were multiplied (e.g.,  $S_o^2 * F_{\text{mono}} * 1 * (\text{non-linear function equations for 3-legged or 4-legged path})$ ).

The outer- and inner-wall of imogolite tubular structures predominantly contain gibbsite-like Al<sub>2</sub>(OH) groups and silanol groups, respectively (Cradwick et al., 1972). Therefore, both U–Al and –Si shells were considered in the initial XAS fit. Several U–Si interatomic distances that have been reported by several other researchers were also considered in the fit, such as bidentate (at  $\sim 2.75$  and  $\sim 3.08$ – $3.15$  Å) and monodentate (at  $\sim 3.66$ – $3.8$  Å) coordination environments (Reich et al., 1996; Moyes et al., 2000; Sylwester et al., 2000). However, these U–Si shells were not successfully fit in all samples, suggesting no U(VI) partitioning reactions into the silanol inner-tubular structure for these reaction conditions.

To facilitate the comparison under different reaction conditions, coordination numbers and Debye–Waller factors for some shells were fixed; (i.e., CN of U–O<sub>eq</sub>: 6,  $\sigma^2$  of U–C:  $0.004$  Å<sup>2</sup>, and  $\sigma^2$  of U–Al:  $0.003$  Å<sup>2</sup>). The  $\sigma^2$  of U–O<sub>dist</sub> MS paths were explicitly calculated from  $\sigma^2$  of SS paths by summing the disorder parameters of each SS path (Hudson et al., 1996). Based on following assumptions  $\sigma_{\text{C-O}}^2 \ll \sigma_{\text{O-dist}}^2 = \sigma_{\text{U-C}}^2 (0.004 \text{ Å}^2)$ ,  $\sigma^2$  for U–O<sub>dist</sub> MS paths was fixed at  $0.004$  Å<sup>2</sup>. The other coordination numbers, Debye–Waller factors, and interatomic distances were allowed to vary unless otherwise mentioned in the text. In order to determine the number of significant components in U(VI) reacted imogolite samples, principal component analysis (PCA) was additionally conducted using  $k^3$ -weighted EXAFS spectra of six adsorption samples at  $3.5$ – $12.4$   $k^{-1}$ .

### 3. Results and discussion

#### 3.1. Ionic strength and pH effects on uranyl adsorption

Fig. 3 shows U(VI) adsorption on the synthetic imogolite as a function of pH and  $U_{\text{tot}}$  concentration. Overall fractional adsorption was insensitive to changes in the total U(VI) concentration at the two lower concentrations studied ( $0.01$  and  $1$  μM) (Fig. 3). U(VI) adsorption increased with increasing pH up to  $\sim 8$ , and decreased with increasing pH from  $8$  to  $10$ . Similar U(VI) adsorption behavior has been reported on various metal oxides such as  $\gamma$ -alumina, ferrihydrite and kaolinite (Prikryl, 1994; Waite et al., 1994; Morrison et al., 1995; Payne et al., 1998, 2001). The distinctive pH-dependent adsorption behavior is attributed to the influence of hydrolysis and carbonate complex formation on U(VI) aqueous speciation. Equilibrium speciation calculations predict that the predominant U(VI) aqueous species are cationic (i.e.,  $UO_2^{2+}$  and  $UO_2OH^+$ ) at  $pH < 6$ , ion pairs (i.e.,  $UO_3CO_3^0$  and  $UO_2(OH)_2^0$ ) at near neutral pH, and anionic complexes (e.g.,  $(UO_2)_2CO_3(OH)_3^-$ ,  $UO_2(CO_3)_2^{2-}$ , and  $UO_2(CO_3)_3^{4-}$ ) at  $pH > 7$  (Figs. 5 and 6). In  $1$  μM U(VI) solution, the aqueous multinuclear species,  $(UO_2)_2CO_3(OH)_3^-$ , is predominant between  $pH$  6.2 and 7.7 (Fig. 6).

Similar pH-dependent U(VI) adsorption is also observed at other ionic strengths (i.e.,  $I = 0.02$  and  $0.5$  M) (Fig. 4). U(VI) adsorption is relatively insensitive to changes in ionic strength at  $pH < 7.5$ , but U(VI) adsorption decreased with increasing  $I$  from  $0.02$  to  $0.5$  M NaNO<sub>3</sub> in the alkaline pH range ( $7.3$ – $10$ ). Waite et al. (1994) showed that ionic strength dependence of U(VI) adsorption in the alkaline pH range can be expected because of the change in activity of the aqueous uranyl-carbonato complexes (Figs. 5 and 6). Because of this, the dependence of adsorp-

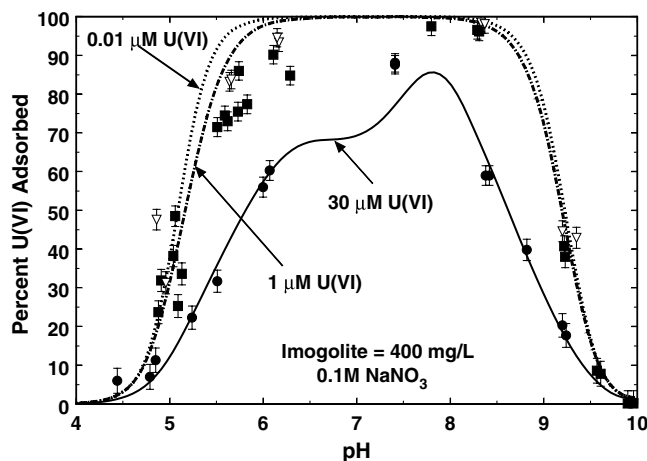


Fig. 3. Experimental and model-calculated percent U(VI) adsorbed as a function of pH and total U(VI) concentration on imogolite ( $400$  mg/L) in  $0.1$  M NaNO<sub>3</sub> solution. Experimental data are shown as symbols (circles =  $30$  μM, squares =  $1$  μM, and downward triangles =  $0.01$  μM  $U(VI)_{\text{tot}}$ ). Model calculations for the corresponding  $U(VI)_{\text{tot}}$  concentrations are shown as solid or dashed curves.

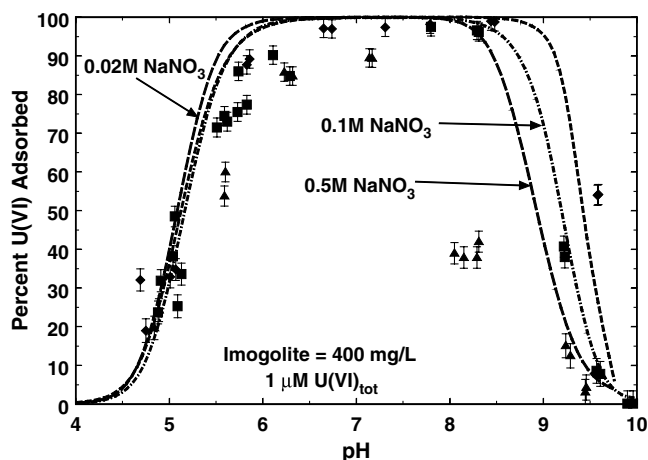


Fig. 4. Experimental and model-calculated percent U(VI) adsorbed as a function of pH and ionic strength on imogolite (400 mg/L) at a total U(VI) concentration of  $1 \mu\text{M}$ . Experimental data are shown as symbols (diamonds = 0.02 M, squares = 0.1 M, and upward triangles = 0.5 M  $\text{NaNO}_3$  solution). Model calculations for the corresponding  $\text{NaNO}_3$  concentrations are shown as dashed or dotted curves.

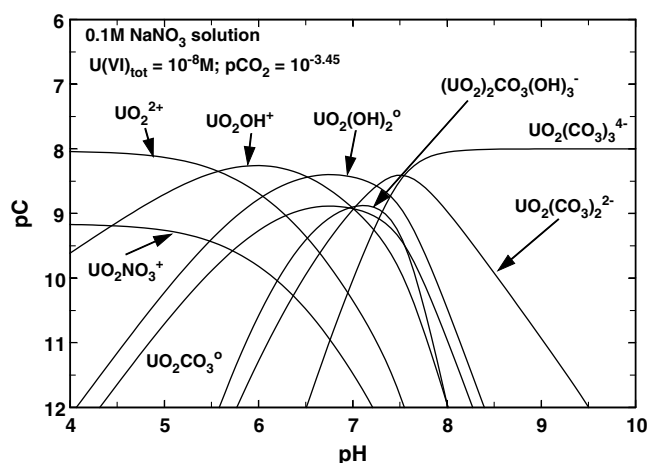


Fig. 5. Aqueous speciation of U(VI) in 0.1 M  $\text{NaNO}_3$  solution in equilibrium with the partial pressure of carbon dioxide ( $p_{\text{CO}_2}$ ) in air ( $10^{-3.45}$  atm); total dissolved U(VI) =  $10^{-8}$  M. Ionic strength = 0.1 for  $\text{pH} < 8.5$ . Ionic strength increases above  $\text{pH} 8.5$  are due to dissolved carbonate. At  $\text{pH} 10$ ,  $I = 0.47$  M. Activity correction made with the Davies equation.

tion on ionic strength in this pH region cannot be used to argue that outer-sphere complexes are the predominant U(VI) surface species. To better understand the U(VI) surface speciation at the imogolite–water interface, we have used an in situ spectroscopic technique, XAS, and the results are discussed below.

### 3.2. Extended X-ray absorption fine structure analyses

Fig. 7a shows the  $k^3$ -weighted EXAFS spectra of U(VI)-adsorbed imogolite samples. Fit results are shown in Table 3 (in units of Å). Interatomic distances mentioned in this section are corrected for phase shift. The structural param-

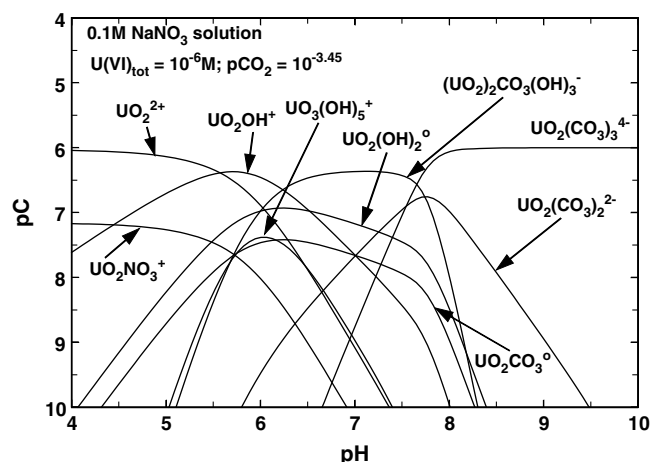


Fig. 6. Aqueous speciation of U(VI) in 0.1 M  $\text{NaNO}_3$  solution in equilibrium with the partial pressure of carbon dioxide ( $p_{\text{CO}_2}$ ) in air ( $10^{-3.45}$  atm); total dissolved U(VI) =  $10^{-6}$  M. Ionic strength = 0.1 for  $\text{pH} < 8.5$ . Ionic strength increases above  $\text{pH} 8.5$  are due to dissolved carbonate. At  $\text{pH} 10$ ,  $I = 0.47$  M. Activity correction made with the Davies equation.

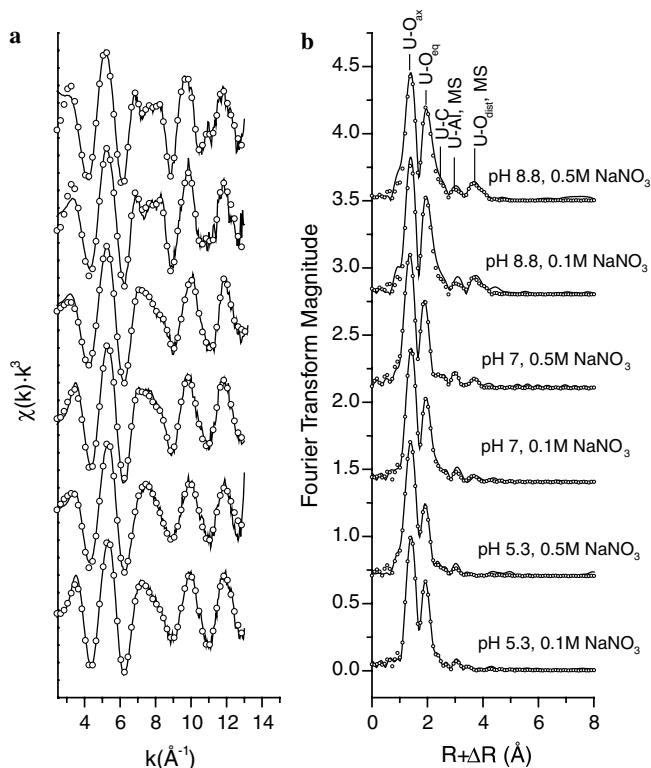


Fig. 7. (a) Normalized, background-subtracted  $k^3$ -weighted U  $L_{\text{III}}$ -edge EXAFS spectra of U(VI) adsorbed imogolite samples are shown. Solid lines are the experimental data and the opened circles represent the theoretical fit to the data. (b) Fourier transformed  $k^3$ -weighted U  $L_{\text{III}}$ -edge EXAFS spectra of U(VI) adsorbed imogolite (solid lines) and nonlinear least-squares fits (open circles) are shown.

eters of all samples contain two axial oxygen distances at approximately  $1.8 \text{ Å}$ , and six equatorial oxygen distances at  $\sim 2.4 \text{ Å}$ , indicating the presence of a  $\text{O}=\text{U}=\text{O}$  trans-dioxo structure. These  $\text{U}-\text{O}_{\text{ax}}/\text{O}_{\text{eq}}$  distances can be clearly

Table 3  
Reaction conditions (pH, ionic strength, initial uranyl concentrations, and loading levels) of XAS samples and structural parameters from the least-squares analyses of U L<sub>III</sub>-edge EXAFS spectra

Reaction condition	Adsorption density		O <sub>ax</sub> (ss)	O <sub>eq</sub>	C	Al	O <sub>dist</sub> (ss)	<i>F</i> <sub>non</sub>	<i>F</i> <sub>mono</sub>	<i>F</i> <sub>bis</sub>	<i>F</i> <sub>tris</sub>	$\beta$ (°)	$\Delta E_o$	Reduced $\chi^2$
pH 8.80, 0.5 M NaNO <sub>3</sub> [U(VI)] <sub>0</sub> =30	0.014	CN	2.0*	6.0*	—	1*	—							
		<i>R</i> (Å)	1.810(7)	2.44(1)	2.90(2)	3.3(1)	4.23(3)	0	0	0.3 ± 0.4	0.7 ± 0.4	176.6*	11 ± 1	34.86
		$\sigma^2$ (Å <sup>2</sup> )	0.0017(3)	0.0063(9)	0.0041*	0.005*	0.004*							
pH 8.82, 0.1 M NaNO <sub>3</sub> [U(VI)] <sub>0</sub> =30	0.18	CN	2.0*	6.0*	—	1*	—							
		<i>R</i> (Å)	1.803(5)	2.431(9)	2.90(2)	3.3(1)	4.22(2)	0	0	0.27 ± 0.4	0.73 ± 0.4	176.6*	13 ± 1	29.26
		$\sigma^2$ (Å <sup>2</sup> )	0.0011(4)	0.0057(6)	0.0041*	0.005*	0.004*							
pH 7.02, 0.5 M NaNO <sub>3</sub> [U(VI)] <sub>0</sub> =6	0.09	CN	2.0*	6.0*	—	1*	—							
		<i>R</i> (Å)	1.800(6)	2.38(1)	2.92(5)	3.32(8)	4.21(5)	0.21 ± 0.4	0	0.78 ± 0.4	0	140*	10 ± 2	88.48
		$\sigma^2$ (Å <sup>2</sup> )	0.0014(5)	0.0074(9)	0.0041*	0.005*	0.004*							
pH 6.94, 0.1 M NaNO <sub>3</sub> [U(VI)] <sub>0</sub> =6	0.09	CN	2.0*	6.0*	—	1*	—							
		<i>R</i> (Å)	1.810(4)	2.416(9)	2.92(3)	3.35(4)	4.25(5)	0.35 ± 0.2	0	0.65 ± 0.2	0	140*	14 ± 1	31.74
		$\sigma^2$ (Å <sup>2</sup> )	0.0013(3)	0.0085(7)	0.0041*	0.005*	0.004*							
pH 5.30, 0.5 M NaNO <sub>3</sub> [U(VI)] <sub>0</sub> =30	0.101	CN	2.0*	6.0*	—	1*	—		0	0.41 ± 0.3	0	180*	10 ± 2	42.78
		<i>R</i> (Å)	1.791(6)	2.37(1)	2.93(5)	3.3(8)	4.3(2)	0.59 ± 0.3						
		$\sigma^2$ (Å <sup>2</sup> )	0.0017(4)	0.010(1)	0.0041*	0.005*	0.004*							
pH 5.26, 0.1 M NaNO <sub>3</sub> [U(VI)] <sub>0</sub> =30	0.28	CN	2.0*	6.0*	—	1*	—	0.69 ± 0.2	0	0.31 ± 0.2	0	180*	13 ± 1	19.23
		<i>R</i> (Å)	1.800(3)	2.391(6)	2.94(3)	3.3(1)	4.3(5)							
		$\sigma^2$ (Å <sup>2</sup> )	0.0018(2)	0.0088(5)	0.0041*	0.005*	0.004*							

[U(VI)]<sub>0</sub>, initial U(VI) concentration (μM); *I*, adsorption density (μM m<sup>-2</sup>); CN, coordination number; *R*, interatomic distance (Å);  $\sigma^2$ , Debye–Waller factor (Å<sup>2</sup>). Fit quality confidence limit for parameters: U–Al shell CN: ±25%, U–Al shell *R*: ±0.02 Å. \*Fixed parameter. Parameters for three U=O<sub>ax</sub> MS paths (*R*: 2 × *R*<sub>Oax</sub> Å,  $\sigma^2$ : 3 ×  $\sigma_{\text{Oax}}^2$ ) and two U–C–O<sub>dis</sub> MS paths (*R*<sub>Odist(ms)</sub>,  $\sigma_{\text{Odist(ms)}}^2$ ) are omitted from the table.



observed in the Fourier Transforms (FTs) at  $\sim 1.5$  and  $2 \text{ \AA}$ ,  $R + \Delta R$  (Fig. 7b). Additional FT peaks are also observed at  $\sim 2.5$ ,  $3.1$ , and  $3.8 \text{ \AA}$ ,  $R + \Delta R$ , which can be attributed to C, Al, and distal O (in carbonate groups) shells, as described below. We did not observe any obvious splitting of U–O<sub>eq</sub> shells in the FTs (Fig. 7b). Further, initial fits were attempted in which the O<sub>eq</sub> shell was split into two shells. These attempts resulted in either convergence of the two shells at the same distance or in trivial improvements in fit quality. Given the data range ( $3.5\text{--}12.4 \text{ \AA}^{-1}$ ) used in these fits, the minimum difference in shell distances that can be resolved is ca.  $0.17 \text{ \AA}$  (Teo, 1986). Thus, the O<sub>eq</sub> shells in the samples under discussion may have been split by distances smaller than  $0.17 \text{ \AA}$  without detection as being split. It has been previously suggested that splitting of the O<sub>eq</sub> shell can be used to infer inner-sphere coordination of U(VI) at water–mineral interfaces. As discussed below, we will rely on the presence of Al backscatters to suggest the presence of inner-sphere surface species.

As reported in the previous XAS study of U(VI) reacted hematite surfaces at  $p_{\text{CO}_2} = 10^{-3.5} \text{ atm}$  (Bargar et al., 2000), the distance at  $\sim 2.5 \text{ \AA}$ ,  $R + \Delta R$ , corresponds to a carbonate ion coordination of the U atom in a bidentate fashion having a U–C distance of  $\sim 2.9 \text{ \AA}$ . This assignment is based largely on the observation that such a distance is too short to be attributed to multiple scattering, Al, or U neighbors, and either too short or too long for O neighbors (Bargar et al., 2000). The FT frequency at  $\sim 3.1 \text{ \AA}$ ,  $R + \Delta R$ , is fit well with Al neighbors at  $\sim 3.3 \text{ \AA}$ , suggesting the formation of inner-sphere bidentate mononuclear surface species on aluminum octahedral structures. Similar U–Al interatomic distances have been reported on montmorillonite surfaces by Hennig et al. (Hennig et al., 2002). The FT frequency at  $\sim 3.8 \text{ \AA}$  is attributed to SS and MS paths of the U–O<sub>dist</sub> at  $\sim 4.2 \text{ \AA}$ . Several researchers have shown the importance of the U–O<sub>dist</sub> distances scattering paths in U(VI)–carbonate minerals (liebigite, cejkaite, rutherfordine, and zellerite) (Catalano and Brown, 2004) and tris-carbonato (aq) species (Bernhard et al., 2001). Our observation of the U–O<sub>dist</sub> contribution from the U(VI) carbonate ternary species at the mineral–water interface and the recent findings by Elzinga et al. (2004) of a carbonate ternary surface species on calcite add new insight into the types of U(VI) surface complexes that may form in low-temperature environments (Elzinga et al., 2004).

To elucidate the number of significant surface species, principal component analyses (PCA) were conducted using  $k^3$ -weighted EXAFS spectra of six adsorption samples. The results are summarized in Table 4. The variance in the sample is largely captured with two components, with only minor improvement with the addition of a third component (Table 4). Spectral reconstructions of the  $0.1 \text{ M NaNO}_3$  spectra are shown in Fig. 8. Two components were sufficient to reproduce the major spectral features in all samples. However, the pH 8.8 sample spectral reconstructions were slightly improved in the spectral range  $7\text{--}9 \text{ \AA}^{-1}$  following the inclusion of the third component

Table 4

Results from principal component analysis of U L<sub>III</sub> edge EXAFS analyses of six U(VI) sorbed imogolite samples

Component, <i>n</i>	Eigen value	Variance explained (%)	Cumulative variance	IND functions
1	74.130	66.9	66.9	0.343
2	15.899	14.3	81.3	0.335
3	7.123	6.4	87.7	0.516
4	5.499	4.9	92.7	1.039
5	5.022	4.5	97.2	3.058
6	3.058	2.7	100	NA

IND function is indicator error function proposed by Malinowski (1991).

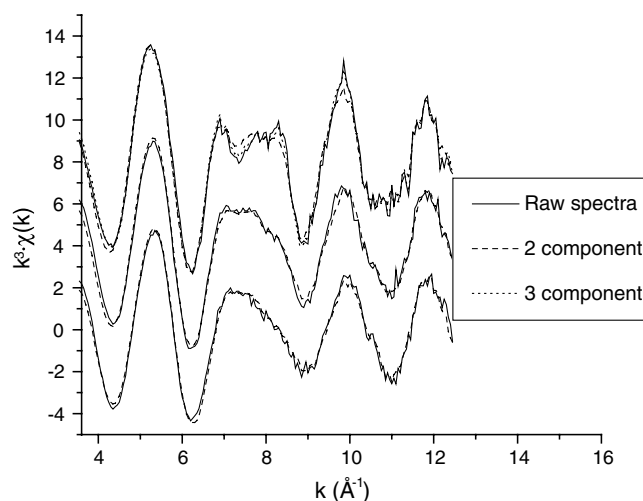


Fig. 8. Principal component and spectra reconstruction analyses of selected U(VI) adsorbed imogolite samples in Table 3 and Figs. 7a and b. The results of spectra reconstruction on samples in  $0.5 \text{ M NaNO}_3$  are not shown.

(Fig. 8). Similar results were obtained for the pH 8.8  $0.5 \text{ M NaNO}_3$  sample. Thus, the PCA suggest the presence of two dominant species. A third minor component cannot be ruled out.

Shell-by-shell fits to the EXAFS spectra were subsequently performed under the assumption, derived from the PCA, that two dominant U(VI) surface species were present. Preliminary analyses indicated the presence of Al neighbors, suggesting the presence of inner-sphere complexes and carbonate ternary ligands. It was thus concluded that the following surface complexes could have been present: binary inner-sphere (i.e., no ternary carbonate ligands present), mono-carbonato inner-sphere, bis-carbonato inner-sphere, and tris-carbonato (outer-sphere surface species). EXAFS fits were initially attempted assuming that two of these four putative species were present.

For the pH 5.3 samples, a combination of binary (59–69%) and bis-carbonato (31–41%) inner-sphere species resulted in the best fit (reduced  $\chi^2$ : 19.23–42.78). When the U–C–O<sub>distal</sub> bond angle (defined here as  $\beta$ ) was varied between  $140^\circ$ ,  $150^\circ$ ,  $160^\circ$ ,  $170^\circ$ , and  $180^\circ$ , negligible changes were observed in reduced  $\chi^2$  values. Final fits assume that  $\beta = 180^\circ$  (Table 3).

At pH 7, U–C and U–Al interatomic distances were observed to be similar to those at pH 5.3 (Table 3). To be consistent with the results of PCA and the pH 5.3 sample fits, we considered a combination of binary and bis-carbonato surface species. The fraction of bis-carbonato inner-sphere surface species slightly increased to 78% as pH increased from 5.3 to 7, with a corresponding decrease in the binary surface species. This pH-dependent increase in the number of carbonate neighbors is consistent with the increase in the activity of solute carbonate anion between pH 5.3 and 7, which is expected to favor the formation of U(VI)-carbonato complexes. Bending  $\beta$  away from  $180^\circ$  rapidly attenuates linear multiple scattering amplitude, resulting in a diminished contribution from the  $4.2 \text{ \AA}$   $O_{\text{distal}}$  shell. To evaluate the sensitivity of the fits to the  $\beta$  angle, the quality of fits (reduced  $\chi^2$  values) were tabulated for  $\beta$  between  $140^\circ$  and  $180^\circ$  in  $10^\circ$  increments. The reduced  $\chi^2$  values slightly improved with decreasing angle from  $180^\circ$  to  $140^\circ$  (32.73–31.74 and 90.03–88.48 for  $I = 0.1$  and  $0.5 \text{ M}$  samples, respectively), suggesting that a bent U–O–C angle might be a preferable configuration for the bis-carbonato surface species at pH 7. The final fits in Table 3 assume a  $\beta$  angle of  $140^\circ$ .

The same combination of surface species (i.e., binary and bis-carbonato ternary species) was used for initial fits to the pH 8.8 samples. As shown in Figs. 10a and b, this combination of species cannot account for the increased amplitude of the C and  $O_{\text{distal}}$  shells at pH 8.8. Various combinations of binary and bis-carbonato species (e.g., binary: 10–30%, and bis-carbonato: 70–90%, cf, Fig. 10) were imposed on the fits in an attempt to conform to the two-component model suggested by the PCA results. In all cases, poor fits were obtained (indicated by arrows in

Figs. 10a and b) because the C and  $O_{\text{distal}}$  shells were clearly underestimated. The increased amplitude in these shells suggests the presence of complexes having three carbonate

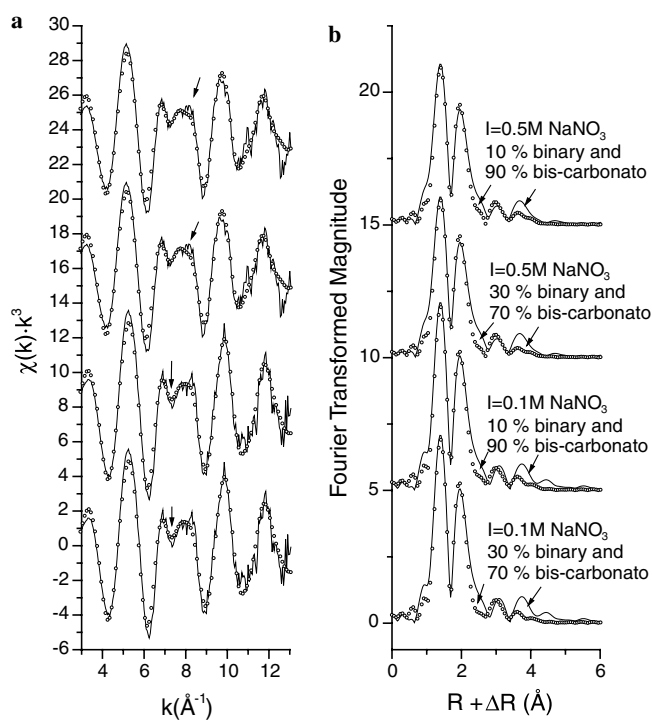


Fig. 10. (a) Normalized, background-subtracted  $k^3$ -weighted U  $L_{\text{III}}$ -edge EXAFS spectra of U(VI) adsorbed imogolite samples at pH 8.8 in 0.1 and 0.5 M  $\text{NaNO}_3$ . (b) Fourier transformed  $k^3$ -weighted U  $L_{\text{III}}$ -edge EXAFS spectra. Solid lines are the experimental data and the opened circles represent the theoretical fit with fixed fractions of binary and bis-carbonato inner-sphere surface species.

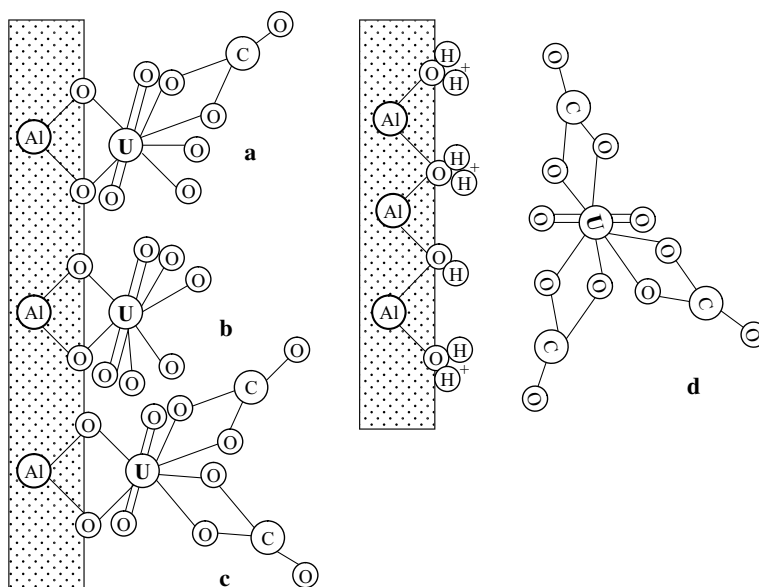


Fig. 9. Ball-and-stick representation of possible U(VI) surface species on the imogolite outer-wall aluminum octahedral structure based on the results of XAS analyses shown in Table 3. (a) U(VI)-monocarbonato ternary complex via bidentate mononuclear U(V)–O–Al linkage. (b) Bidentate mononuclear binary U(VI) surface complex. (c) bis-Carbonato U(VI) ternary complex via bidentate mononuclear U(VI)–O–Al linkage. (d) Planar tris-Carbonato U(VI) outer-sphere surface complex (with three carbonate groups facing the surface of the imogolite outer wall).

ligands, which we interpret as outer-sphere species. U(VI) tris-carbonato species were subsequently considered in the fits. When these three species were considered, the model consistently rejected the binary species, and the combination of bis-carbonato inner-sphere and tris-carbonato outer-sphere surface species produced the best fit result (reduced  $\chi^2 = 29\text{--}35$ ) with the  $\beta$  angle of  $176.6^\circ$  for both pH 8.8 samples (Table 3). This result implies the presence of three types of surface complexes, i.e., binary, bis-, and tris-carbonato, in partial contradiction of the PCA results. To reconcile the shell-by-shell fitting and PCA results, we note that the tris-carbonato species modifies the shapes of the EXAFS spectra in the  $7\text{--}9\text{ \AA}^{-1}$  range (Fig. 10), which is exactly the range where a third PCA component was found to enhance the spectral reconstructions of the pH 8.8 samples. Further, we note that the C and O<sub>distal</sub> shells' overall contribution to the EXAFS amplitude is relatively minor, particularly when comparing bis- and tris-carbonato species. Whereas the presence of the latter species is clearly distinguished in the FTs, the whole-spectrum PCA approach, which sums over all frequencies including the spectral noise and spline subtraction errors, is only weakly sensitive to changes in the number of carbonate ligands. During the final fits to the pH 8.8 samples, the  $\beta$  angle was fixed at  $176.6^\circ$  to reduce the number of variables. The fraction of bis-carbonato inner-sphere surface species and tris-carbonato outer-sphere surface species was approximately  $30 \pm 0.4\%$  and  $70 \pm 0.4\%$ . Average  $\beta$  angle of bis- and tris-carbonato surface species indicates that U(VI)-carbonato surface species are nearly planar with respects to the  $x\text{--}z$  plane (Fig. 1). The schematic molecular configuration of bis-carbonato inner-sphere and outer-sphere tris-carbonato surface species is shown in Figs. 9c and d, respectively. Although the distribution between the two species at the two different ionic strengths might not be significantly different when the error values ( $\pm 0.4$ ) are considered, a slight reduction in % outer-sphere surface species at higher ionic strength agrees with the macroscopic observation at pH  $> 7$  (Fig. 4). Evidence for a U(VI) outer-sphere species on smectite surfaces was previously shown using EXAFS, Raman vibrational, and time-resolved emission spectroscopies (Dent et al., 1992; Morris et al., 1994), and our XAS analyses further support the evidence for U(VI) outer-sphere surface species on phyllosilicate mineral surfaces.

### 3.3. Surface complexation modeling

#### 3.3.1. Imogolite surface sites

Imogolite is a tubular 1:1 aluminosilicate whose structure has been described by Gustafsson (2001) and Cradwick et al. (1972). Imogolite tubes have a wall composed of a single continuous sheet with gibbsite-like structure, with the inner hydroxyl surface replaced by O<sub>3</sub>SiOH groups (Farmer et al., 1983). Nuclear magnetic resonance studies have shown that essentially all Al in the structure is in hexavalent coordination and all Si is present in unpo-

lymerized, tetravalent coordination (Goodman et al., 1985; Ildefonse et al., 1994). The formation of imogolite is believed to occur in the gibbsite sheet through the displacement of three hydroxyl groups surrounding a vacant octahedral site by an orthosilicate anion (Gustafsson, 2001). The resulting shortening of the oxygen–oxygen bond distances around the site causes the gibbsite sheet to curl and form a tube. The typical inner tube diameter is 1.0 nm, the outer tube diameter may vary from 2.0 to 2.7 nm, and a typical tube length is 2–3  $\mu\text{m}$ . All hydroxyls that are bonded to Al atoms on the outer wall are doubly coordinated; singly coordinated hydroxyls are found only at the tube ends (Gustafsson, 2001). Imogolite precipitates are not observed as single fibers; bundles of fibers with close hexagonal packing have been described by a number of authors (Hoshino et al., 1996; Pohl et al., 1996; Davis, 2001).

Assuming a typical outer-sphere diameter of 2.3 nm for synthetic imogolite tubes, the ratio of outer tube surface area to inner tube surface area should be equal to the ratio of the radii  $= 1.15 \div 5 = 2.3$ . The surface area of the tube ends constitutes only a very small portion of the surface area, on the order of 0.1% assuming a typical tube length of 2.5  $\mu\text{m}$ . The outer surface wall of the tube, which is gibbsite-like, should constitute about 70% of the imogolite surface area. Although the BET surface area was measured at  $166\text{ m}^2/\text{g}$  in this study, it is known from ethylene glycol monoethyl ether (EGME) measurements that the surface areas of synthetic imogolite preparations are considerably greater, perhaps as high as  $900\text{--}1000\text{ m}^2/\text{g}$ . (Harsh et al., 2002).

The total number of hydroxyl surface sites was estimated by tritium exchange to be  $0.0126\text{ mol/g}$  for the synthetic imogolite used in this study (Davis, 2001). The gibbsite structure has 12 hydroxyl sites/ $\text{nm}^2$  on the basal plane (Parfitt and Russel, 1977), so assuming this value for the imogolite outer wall and 7.9 hydroxyl sites/ $\text{nm}^2$  for the silicate inner wall (Koretsky et al., 1998), yields the following equations normalized to 1 g of imogolite (assuming that edge sites make a negligible contribution to the total sites):

$$X + Y = 0.0126\text{ mol} = 7.61 \times 10^{21}\text{ sites}, \quad (1)$$

$$\text{Gibbsite (outer tube) area (m}^2\text{)} = X \div 1.2 \times 10^{19}, \quad (2)$$

$$\text{Silicate (inner tube) area (m}^2\text{)} = Y \div 7.9 \times 10^{18}, \quad (3)$$

where  $X$  = gibbsite sites/g and  $Y$  = silicate sites/g. Since the gibbsite area is 2.3 times greater than the silicate area (see above), then:

$$(7.9 \times 10^{18})X = (2.3)(1.2 \times 10^{19})Y, \quad \text{or} \quad X = 3.494Y. \quad (4)$$

Combining Eqs. (1) and (4) and solving,  $X = 5.915 \times 10^{21}$  gibbsite(outer tube) sites and  $Y = 1.693 \times 10^{21}$  silicate(inner tube) sites, per gram of imogolite. This is equivalent to  $493\text{ m}^2$  of gibbsite surface area and  $214\text{ m}^2$  of silicate surface area, per gram of imogolite, and yields an estimated total surface area of  $707\text{ m}^2/\text{g}$ , in reasonable agreement with the high surface areas of imogolite samples measured by the EGME method.

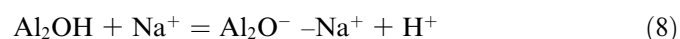
Since the EXAFS results suggest that only the gibbsite surface formed uranyl surface complexes, the “total” surface site density used in the modeling was that of the gibbsite portion (493 m<sup>2</sup>/g) of the imogolite surface area, with the specific site density of 12 sites/nm<sup>2</sup>. Since all of the experiments were conducted with 400 mg/L of imogolite, this corresponds to a site density of 3.934 mmol of gibbsite surface hydroxyl groups per liter of solution.

### 3.3.2. Electrical double layer

Since U(VI) surface complexes were only observed with the outer gibbsite-like layer, the EDL parameters applied in surface complexation modeling were those estimated for a gibbsite surface, and it was assumed that the EDL within the imogolite tubes did not influence that observed on the outer walls of the tubes. A PZC value of 9.8, delta pK value of 5.6 (for surface acidity constants), and inner and outer layer capacitance values of 0.6 F/m<sup>2</sup> were adopted from the analysis of Sverjensky (2005). Following the conventions of Sverjensky (2005) for surface area and site density corrections from the standard state yields acidity constants of 5.2 and –14.4 for log  $K_{a1}$  and log  $K_{a2}$ , respectively, for the equations:



The constants for electrolyte binding are 7.9 and –11.5 for log  $K_{\text{nitrate}}$  and log  $K_{\text{sodium}}$ , respectively, after surface area and site density corrections from the standard state (Sverjensky, 2005) for the equations:



Although the acidity of the outer gibbsite-like layer could also be modeled with a single reaction (Hiemstra et al., 1989) rather than both Eqs. (5) and (6), recent EDL comparison studies have shown that the one- and two-reaction approaches for surface acidity yield similar results (Piascecki, 2002). The self-consistency of the Sverjensky (2005) analysis and model parameterization, which is based on multiple gibbsite datasets, offers an advantage for this study, in that the EDL model parameters do not need to be derived from data fitting.

### 3.3.3. Bond-valence analysis

The relative stabilities (or instabilities) of putative imogolite surface sites and complexes can be assessed using the bond-valence approach (Bargar et al., 1997). Bond valence ( $v$ , valence units) is a measure of the strength of individual cation–anion bonds, which is calculated from the ion coordination number and bond length (Brese and O’Keefe, 1991). The term, *bond valence*, is used here to avoid confusion with the classical Pauling definition of bond strength. The central tenet of this approach is the bond-valence rule, which states that, in stable structures, the sum of bond valences to a given metal or oxygen from its surrounding

neighbors should obtain a value close to the formal valence of the central cation (or to the absolute value of the formal valence of a central anion).

Since imogolite is believed to be terminated by (hydr)-oxo groups (Cradwick et al., 1972), we focus on surface oxygens to assess stabilities of surface species. A surface oxygen is said to be coordinatively oversaturated and unstable if its bond-valence sum ( $\Sigma v$ ) obtains values significantly greater than 2.0 v.u. Surface oxygen species for which  $\Sigma v$  is less than 2.0 v.u. (coordinatively undersaturated) cannot be ruled out, but are likely to be reactive and thus unstable relative to oxygen species having bond-valence sums near 2.0 v.u. (Bargar et al., 1997).  $\text{Al}^{3+}$  and  $\text{Si}^{4+}$  are explicitly assumed to obtain their complete coordination spheres (i.e., maintain coordinative saturation) because of their high charge/radius ratios and the abundance of (hydr)-oxo and water species to which they may coordinate.  $v_{\text{Al-O}}$  and  $v_{\text{Si-O}}$  were calculated from the Al–O and Si–O bond distances reported for imogolite (Cradwick et al., 1972) using the parameters from Brese and O’Keefe (1991). For  $\text{O}-\text{UO}_2^{2+}$  bonds, a  $v_{\text{U-O}}$  value of 0.5 v.u. was used, which is obtained from the EXAFS-derived average U–O<sub>eq</sub> distance of 2.39 Å (i.e., from the pH 5.3 and 7 samples, which are dominated by the inner-sphere surface complexes), and using the recently refined  $\text{UO}_2$  bond-valence parameters (Burns et al., 1997). Following the arguments presented in Bargar et al. (1997), hydroxide ion bond valences are assumed to exhibit values ranging from  $0.68 \leq v_{\text{OH}} \leq 0.88$  v.u. and hydrogen bonds are expected to exhibit values between  $0.13 \leq v_{\text{OH}} \leq 0.25$  v.u. Oxygens are assumed to have a maximum coordination number of 4, based on the coordination chemistry of metal hydrates, ice, and aqueous solutions. It should be noted that the predicted surface species are further subject to steric and thermodynamic constraints not explicitly accounted for by bond valence. Therefore, a surface species predicted to be stable from a bond-valence perspective may occur at negligible concentrations due to a lack of reactants, the presence of more stable species, or unfavorable kinetics.

Bond-valence analyses for surface species are summarized in Table 5. In calculating  $\Sigma v$  values for these sites, it was necessary to account for the likely relaxation of the local surface structure upon deprotonation or coordination of metal cations. The relevant atomic surface structures are not known, and it is thus necessary to allow for a range of bond lengths (and angles) at the surface sites. Accordingly, the values reported in Table 5 explicitly assume that Al–O and Si–O bond lengths can contract or expand within the limits reported for imogolite ( $1.83 \leq r_{\text{Al-O}} \leq 2.0$  Å;  $1.58 \leq r_{\text{Si-O}} \leq 1.72$  Å), a relatively large range of distances for each cation, in order to attempt to achieve stable configurations (i.e.,  $\Sigma v = 2.0$  v.u. for surface oxygens). As shown in Table 5, the  $\Sigma v$  calculations predict that SiOH (tube interiors and ends),  $\text{Al}_2\text{OH}$  (tube exteriors), and  $\text{AlOH}_2^+$  (tube ends) are the most stable surface sites, in general agreement with the published crystal structure.



Table 5  
Bond-valence analyses for functional groups and potential U(VI)-surface conformations on imogolite

	$\Sigma v$ at Oxygen (valence units—v.u.)			
	No H-bonds	With H-bonds	Oxygen bonding state	Expected stability
<i>Interfacial sites</i>				
Tunnel interior				
Si—OH	≤2.01	1.71–2.51	Saturated	Stable
Si—O <sup>−</sup>	≤1.13	≤1.88	Unsaturated	Plausible
External tube surfaces				
Al <sub>2</sub> —OH	1.46–2.12	1.59–2.37	Saturated	Stable
Al <sub>2</sub> —O <sup>−</sup>	≤1.24	≤1.74	Unsaturated	Plausible
Tube end sites				
Si—OH	≤2.01	1.71–2.51	Saturated	Stable
Si—O <sup>−</sup>	≤1.13	≤1.88	Unsaturated	Plausible
Al—OH <sub>2</sub> <sup>+</sup>	1.75–2.38	1.88–2.63	Saturated	Stable
Al—OH	≤1.50	≤2.00	Saturated <sup>b</sup>	Stable <sup>b</sup>
<i>Surface complexes: Me—O(H)—UO<sub>2</sub> linkages<sup>a</sup></i>				
Tunnel interior				
Si—O—UO <sub>2</sub>	≤1.63	1.53–2.13	Saturated	Stable
Si—OH—UO <sub>2</sub>	≥1.95	≥2.08	Saturated	Stable <sup>c</sup>
External tube surfaces				
Al <sub>2</sub> —O—UO <sub>2</sub>	≤1.74	≤1.99	Saturated <sup>b</sup>	Plausible
Al <sub>2</sub> —OH—UO <sub>2</sub>	≥1.96	≥1.96	Saturated	Stable
Tube end sites				
Si—O—UO <sub>2</sub>	≤1.63	1.53–2.13	Saturated	Stable
Si—OH—UO <sub>2</sub>	≥1.95	≥2.08	Saturated	Stable <sup>c</sup>
Al—OH <sub>2</sub> —UO <sub>2</sub>	≥2.25	≥2.25	Oversaturated	Should not occur
Al—OH—UO <sub>2</sub>	1.57–2.00	1.70–2.25	Saturated	Stable
Al—O—UO <sub>2</sub>	≤1.12	≤1.62	Unsaturated	Plausible

<sup>a</sup> The total charge on the surface complex depends upon the number of surface sites involved.

<sup>b</sup> This condition is valid only under conditions of maximum bond contraction.

<sup>c</sup> This group is stable when it does not accept an H bond.

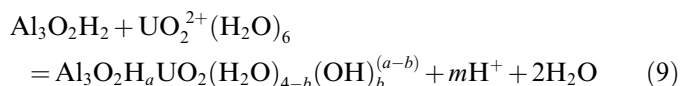
Bond-valence analyses for U(VI)-surface bonding conformations are listed in the bottom half of Table 5. From a bond-valence perspective, the most stable bonding conformations for the spatially dominant inner and outer tube surfaces are predicted to be surface Si–O–UO<sub>2</sub> and Al<sub>2</sub>–OH–UO<sub>2</sub>. Both arrangements may be present multiple times in multidentate/multimeric surface complexes. Surface Si–OH–UO<sub>2</sub> and Al<sub>2</sub>–O–UO<sub>2</sub> linkages cannot be ruled out, but are likely to be more reactive and thus less stable than the forgoing conformations because they require maximal distortion of Me–O and O–H bond lengths to satisfy the bond-valence sum rule. On tube ends, the most stable U(VI)-surface bonding conformations are predicted to be Si–O–UO<sub>2</sub> and Al–OH–UO<sub>2</sub>.

### 3.3.4. Uranium(VI) surface species

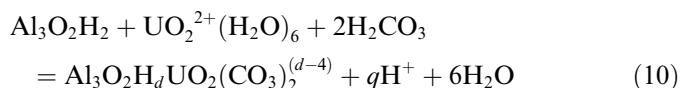
The selection of U(VI) surface reactions was based on the spectroscopic results and bond-valence analysis. Since the U(VI) adsorption density was relatively high in the samples prepared for spectroscopic analysis, the macro-

scopic adsorption/pH curve at 30  $\mu$ M total U(VI) was used for surface complexation fitting because of the similar range in U(VI) surface coverage to the XAS samples.

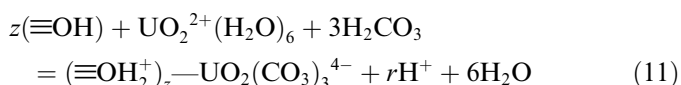
The EXAFS spectroscopic analyses indicated that there were at least three surface complexes formed on the imogolite surface: (1) an inner-sphere, uranyl-surface binary complex (non-carbonated species), (2) an inner-sphere, ternary bis-carbonato uranyl-surface complex, and (3) an outer-sphere, tris-carbonato uranyl-surface complex (Table 3). At the high adsorption density measured in the adsorption/pH curve at 30  $\mu$ M total U(VI), it can be assumed that imogolite edge sites make a negligible contribution to the measured U(VI) adsorption because of their small abundance (see discussion above). Two adjacent surface hydroxyls are involved in each inner-sphere bond. Because each hydroxyl is doubly coordinated to aluminum atoms on the gibbsite basal plane, the bidentate surface complexes involve three aluminum atoms. Formation of the binary uranyl-surface reaction can be written generally as follows:



where  $m = 2 - a + b$ . Based on observations of metal binding with carbonate in aqueous complexes and in mineral structures, it is assumed that carbonate ligands are unprotonated in the surface complexes involving the carbonate ligand, and formation of the bis-carbonato inner-sphere reaction can be written generally as follows:



where  $q = (6 - d)$ . The tris-carbonato outer-sphere complex formation reaction can be written as follows:



where  $r = (6 - z)$ .

The proton stoichiometry of reactions (9)–(11) cannot be determined from EXAFS spectroscopic results. However, bond-valence calculations suggest that the gibbsite surface oxygen atoms that are bonded to U could be protonated or unprotonated, with acceptance of a hydrogen bond in the latter case. The proton stoichiometry of the reactions affects both the slope of the adsorption/pH curve and the pH range over which the surface species predominates. For example, at pH 5.3, EXAFS analysis indicated that adsorbed U(VI) was present predominantly as the binary uranyl-surface complex (reaction (9)). Trial-and-error FITEQL calculations were made to compare the slope of calculated adsorption with this species with the experimental data in the pH range 4.4–6.2 with the proton coefficient,  $m$ , on the right-hand side of Eq. (9) equal to 1, 2, 3 or 4 (Fig. 11). The best fits to the pH dependence of the U(VI) adsorption data in this pH range were obtained with  $m = 2$  or 3, but it can also be seen that the choice of



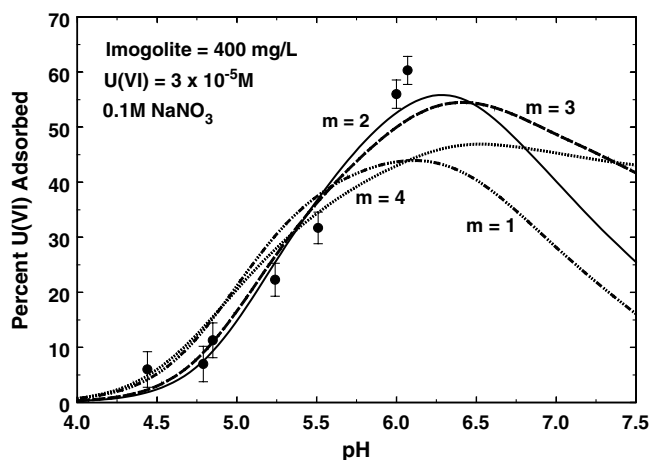


Fig. 11. Comparison of model calculations and experimental data for U(VI) adsorption on imogolite with reaction (9) (inner-sphere, binary uranyl-surface complex) and various values of the proton stoichiometric coefficient,  $m$ .

the proton coefficient also affects the calculated adsorption at higher pH values (e.g., pH 7).

At pH 7, the spectroscopic data suggest that the ternary bis-carbonato surface complex (reaction (10)) predominates and is also a significant species at pH values 5.3 and 8.8 (Table 3). FITEQL calculations were made to compare the slope of calculated adsorption with this species with the experimental data in the pH range 7–9.3 with the proton coefficient,  $q$ , on the right-hand side of Eq. (10) equal to 4, 5 or 6 (Fig. 12). The calculations suggest that the best fits to the pH dependence of the U(VI) adsorption data in the pH range 7–9.3 are obtained with  $q = 4$  or 5 for reaction (10), but the calculations also show that the predicted U(VI) adsorption at low pH is much greater than the experimental observations. If  $q = 4$ , then  $d = 2$  in reaction (10), and the net charge on the surface species is  $-2$ . In the calculations shown in Fig. 11, the charge on the bis-carbonato species was assumed to be located

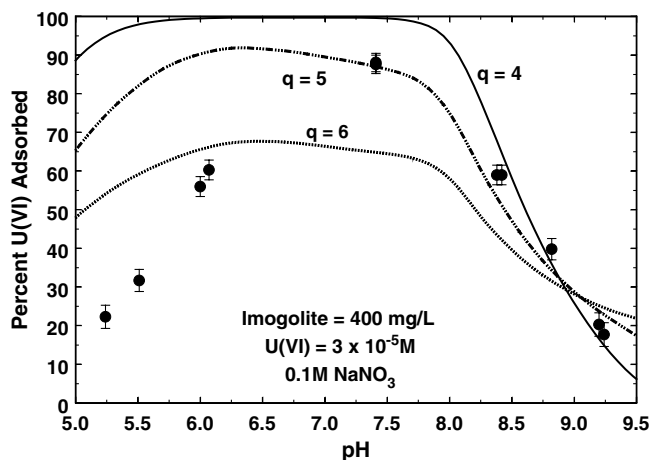


Fig. 12. Comparison of model calculations and experimental data for U(VI) adsorption on imogolite with reaction (10) (inner-sphere, uranyl bis-carbonato surface complex) and various values of the proton stoichiometric coefficient,  $q$ .

in the  $\sigma_o$  plane for the purposes of formulating the electrostatic attraction term of the mass law. Some or all of the negative charge of this species may be localized near the oxygen atoms of the carbonato groups, and the carbonato groups are located at much greater distance from the surface than uranium in this ternary complex. Thus, even though an inner-sphere species is formed, the charge may be localized closer to the  $\sigma_\beta$  plane than the  $\sigma_o$  plane. Fig. 13 shows FITEQL calculations that compare calculated adsorption for the ternary bis-carbonato surface complex (reaction (10)) with the proton coefficient,  $q$ , equal to 4 and with the charge in the  $\sigma_o$  plane equal to  $-2$ ,  $-1.5$ ,  $-1$ ,  $-0.5$ , and  $0$ . For each calculation, the balance of the net charge ( $-2$ ) for the species was located in the  $\sigma_\beta$  plane,  $0$ ,  $-0.5$ ,  $-1$ ,  $-1.5$ , and  $-2$ , respectively. The calculations illustrate that the pH slopes of the calculated curves in the pH range 8–9 are only slightly affected by the assumed distribution of charge between the planes; however, the distribution has a very large effect on the calculated adsorption at lower pH. The results show that both the proton stoichiometry and the distribution of species charge have a large effect on the predicted pH dependence of adsorption for this species. With the charge distributed evenly between the two planes ( $-1$  in each plane), the calculated curve agrees well with the experimental adsorption data over the entire pH range (Fig. 13).

At pH 8.8, the spectroscopic data suggest that an outer-sphere, tris-carbonato surface complex (reaction (11)) predominates (Table 3). Since the aqueous uranyl-tris-carbonato species has a planar structure, it seems likely that such a species would align parallel to the surface and interact with several positively charged surface hydroxyls. Fig. 14 shows FITEQL calculations that were made to compare the slope of calculated U(VI) adsorption with the outer-sphere, tris-carbonato surface species with the

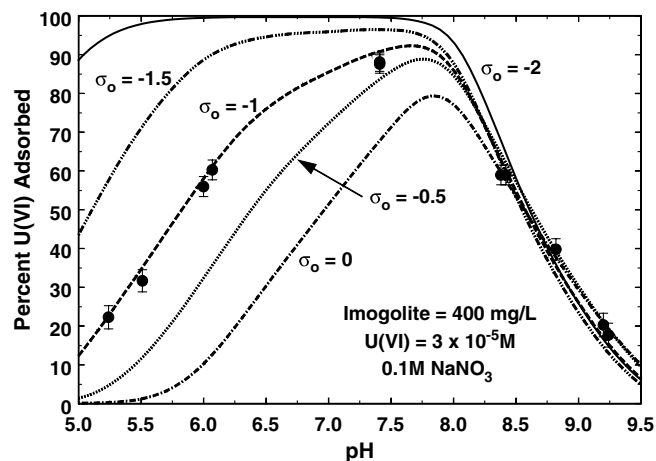


Fig. 13. Comparison of model calculations and experimental data for U(VI) adsorption on imogolite with reaction (10) (inner-sphere, uranyl bis-carbonato surface complex), with the proton stoichiometric coefficient,  $q$ , equal to 4, and for various distributions of the net surface species charge ( $= -2$ ) between the  $\sigma_o$  and  $\sigma_\beta$  planes. Curves are denoted by the charge in the  $\sigma_o$  plane; the balance of charge was placed in the  $\sigma_\beta$  plane.

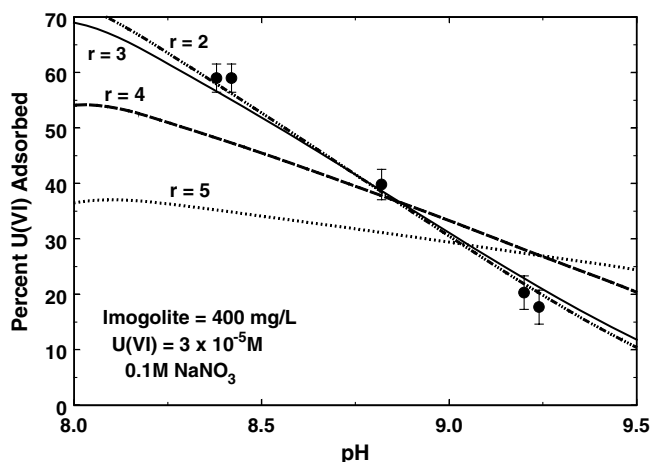


Fig. 14. Comparison of model calculations and experimental data for U(VI) adsorption on imogolite with reaction (11) (outer-sphere, uranyl tris-carbonato surface complex) and various values of the proton stoichiometric coefficient,  $r$ .

experimental data in the pH range 8.3–9.2 with the proton coefficient,  $r$ , on the right-hand side of Eq. (11) equal to 2, 3, 4, or 5. The calculations illustrate that the pH dependence of the calculated adsorption of this species is weak in comparison to the data if  $r = 4$  or 5. The results suggest that  $r = 2$  or 3, and since  $r = 6 - z$ , it suggests that the complex interacts with 3 or 4 positively charged aluminol groups, mostly likely via hydrogen bonding.

The calculations described above (Figs. 11–14) were made with individual surface species, to illustrate the effects of proton stoichiometry and charge distribution on calculated U(VI) adsorption. The next step is to consider the three surface species simultaneously; competitive sorption among the species will affect the calculated pH dependence of macroscopic U(VI) adsorption, the surface charge, and the pH regions of predominance for individual surface species. Preliminary calculations showed the outer-sphere, tris-carbonato complex was an important species at pH 7 if  $r = 2$  (reaction (11)), so the value of  $r = 3$  was selected for subsequent calculations. The proton coefficient in (reaction (10)),  $q$ , was selected to have a value of 4 for subsequent calculations because calculated U(VI) adsorption was too large in the pH region 9–9.5 if  $p = 5$  or 6 (Fig. 12). With  $q = 4$  in (reaction (10)), then  $d = 2$ , indicating that the surface oxygen atoms remain protonated during formation of the inner-sphere bis-carbonato ternary surface complex. Monocarbonato ternary surface complexes were not identified by the EXAFS spectroscopy, so this species was not included in model calculations. For reaction (9),  $m$  was selected to have a value of 2 because the binary uranyl-surface complex became too important at pH 7 (in comparison to the bis-carbonato ternary complex) if  $m$  had a value of 3. With  $m = 2$ , then  $a = b$  in reaction (9), and this species is uncharged.

Fig. 15 shows the final fit of the three-species model to the experimental adsorption data at  $U(VI)_{\text{tot}} = 30 \mu\text{M}$ . With the proton coefficient values set for each equation

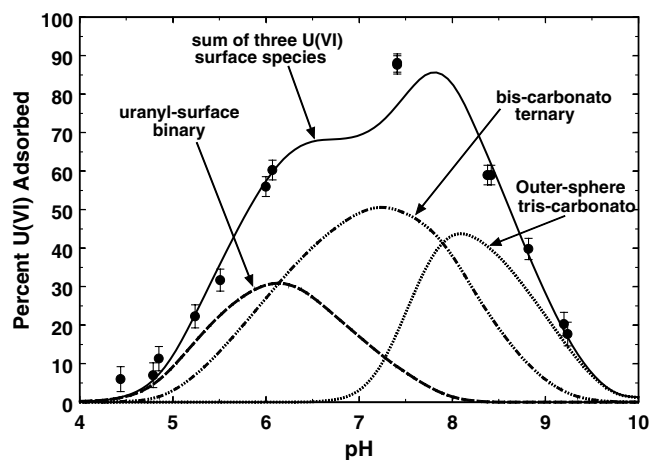


Fig. 15. Final surface complexation model showing the calculated U(VI) adsorption as a function of pH (solid curve) in comparison to the experimental data (400 mg/L imogolite, 30  $\mu\text{M}$   $U(VI)_{\text{tot}}$ , 0.1 M  $\text{NaNO}_3$  solution, equilibration with air). The calculated U(VI) adsorption is equal to the sum of the three U(VI) surface species whose calculated concentrations as a function of pH are each shown as dashed and/or dotted curves. Note the relatively good agreement of the calculated species distribution with the species distribution at the pH values determined by XAS spectroscopy (Table 3).

as described above, the only remaining variables to be determined were the stability constants for each reaction (Eqs. (9)–(11)) and the charge distribution for reaction (10). A value for the charge distribution of the bis-carbonato complex ( $\sigma_o = -1.1$ ;  $\sigma_\beta = -0.9$ ) was selected by comparing the consistency of calculated model output with both the distribution of surface species at pH 7 (Table 3) and the experimental U(VI) adsorption data (Fig. 15). Once the value for the charge distribution for reaction (10) was constrained, FITEQL was used to determine the stability constants for the reactions by optimizing the fit of the model output to the adsorption data (Fig. 15). Table 6 gives the stoichiometry and values of the stability constants for each surface reaction of the model. The model yields calculated values for overall U(VI) adsorption and individual surface species that are in excellent agreement with both the macroscopic uptake data and the spectroscopic analysis of species at different pH values.

### 3.3.5. Surface complexation model at low U(VI) concentrations

Fig. 3 shows that the percent U(VI) adsorbed increased at low U(VI) concentrations, indicating that the U(VI) adsorption isotherm on imogolite is non-linear (slope less than one). Many other investigators have interpreted this behavior as indicative of strong and weak sites on oxide adsorbents. Edge sites represent a very small fraction of the imogolite surface area ( $\sim 0.04\%$ ); and U(VI) adsorbed on the edge sites would not contribute significantly to the EXAFS absorption spectra at the U(VI) adsorption densities observed in the XAS samples. Thus, the identity of U(VI) surface species at the edge sites is not known.

Table 6  
Surface complexation reaction stoichiometry and formation constants

Surface species	Exponents in mass law defining the surface species <sup>*</sup>								log $K_f$ ( $I = 0$ )
	a	b	c	d	e	f	g	h	
$\text{Al}_2\text{OH}_2^+$	1	1					1		5.20
$\text{Al}_2\text{O}^-$	1	–1					–1		–14.40
$\text{Al}_2\text{OH}_2^+ - \text{NO}_3^-$	1	1				1	1	–1	7.90
$\text{Al}_2\text{O}^- - \text{Na}^+$	1	–1			1		–1	1	–11.50
$(\text{Al}_2\text{O}_{\text{outer}})_2\text{UO}_2$	2	–2		1					–5.44
$(\text{AlOH}_{\text{edge}})_2\text{UO}_2(\text{CO}_3)_2^{2-}$	2	–4	2	1			–1.1	–0.9	–2.19
$(\text{Al}_2\text{OH}_{\text{outer}})_2\text{UO}_2(\text{CO}_3)_2^{2-}$	2	–4	2	1			–1.1	–0.9	–9.56
$(\text{Al}_2\text{OH}_2^+)_3 - \text{UO}_2(\text{CO}_3)_3^{4-}$	3	–3	3	1			3	–4	8.62

<sup>\*</sup> Mass law for formation of the surface species is:  $[\text{Surface species}] = K_f [\text{Al}_2\text{OH}]^a (\text{H}^+)^b (\text{H}_2\text{CO}_3)^c (\text{UO}_2^{2+})^d (\text{Na}^+)^e (\text{NO}_3^-)^f \exp \{(-F/RT)(g\Psi_o + h\Psi_\beta)\}$ .

Assuming that U(VI) surface reactions with the outer alumina surface (and associated stability constants) are known from the modeling shown in Fig. 15, FITEQL was used to determine the optimum strong site density to fit the experimental data at a total U(VI) concentration of 0.01  $\mu\text{M}$ , assuming that the distribution of U(VI) surface species with pH was the same as that observed at the 30  $\mu\text{M}$  total U(VI) concentration. The results indicated that the optimum value for the strong site density was 0.03% of the total sites. Given that the edge site density is estimated to be equal to 0.04% of the total sites, it was assumed that the stronger bonding observed at low U(VI) sites was on aluminol edge sites. It was found that a satisfactory description of the adsorption behavior at the 0.01  $\mu\text{M}$  total U(VI) concentration could be obtained with just the bis-carbonato species reacting with the edge sites, so in the absence of spectroscopic data at these low U(VI) adsorption densities, this parsimonious modeling approach was adopted. The fit to the experimental data at the 0.01  $\mu\text{M}$  total U(VI) concentration is shown in Fig. 3 and the edge site stability constant is given in Table 6. Model agreement with the experimental data for a total U(VI) concentration of 1  $\mu\text{M}$  is also shown in the figure; this calculation is a prediction at the intermediate U(VI) concentration, without further optimization of model parameters.

Fig. 4 shows the agreement between model predictions and experimental data as a function of ionic strength at a total U(VI) concentration of 1  $\mu\text{M}$ . The predictions are good at  $\text{NaNO}_3$  concentrations of 0.02 and 0.1 M, but relatively poor at 0.5 M  $\text{NaNO}_3$ . The experimental data show that U(VI) adsorption decreased at the higher ionic strength to a much greater degree than the model predicts. The reason for the larger decrease in U(VI) adsorption at the high ionic strength is unknown, but it is likely that the decrease is due to the formation of poorly understood aqueous species, i.e.,  $\text{Na}_3\text{UO}_2(\text{CO}_3)_3^-$ ,  $\text{Na}_4\text{UO}_2(\text{CO}_3)_3^0$  (Guillaumont et al., 2003, p. 670). These authors have noted that in studies of the aqueous species,  $\text{Ca}_2\text{UO}_2(\text{CO}_3)_3^0$  (e.g., Bernhard et al., 2001), there is an unexplained dependence of the stability constant on  $\text{Na}^+$  concentration that is likely due to the formation of  $\text{Na}_x\text{UO}_2(\text{CO}_3)_3^{x-4}$  aqueous species. A recent study (Fox et al., 2006) has shown that the  $\text{Ca}_2\text{UO}_2(\text{CO}_3)_3^0$  species does not adsorb, and by chem-

ical analogy it can be argued that the  $\text{Na}_x\text{UO}_2(\text{CO}_3)_3^{x-4}$  aqueous species also do not adsorb. Thus, in 0.5 M  $\text{NaNO}_3$  solution, U(VI) adsorption on imogolite is likely decreased in the pH range 7–9 (Fig. 4) due to formation of the  $\text{Na}_x\text{UO}_2(\text{CO}_3)_3^{x-4}$  aqueous species. Since these species were not considered in the modeling due to the lack of formation constants, the adsorption of U(VI) at high pH is likely over-predicted in 0.5 M  $\text{NaNO}_3$  solution at alkaline pH values.

The surface complexation modeling approach used in this study differs from previous approaches, in that priority was given to selecting surface species that were consistent with independent spectroscopic measurements. Most other surface complexation models in the literature have been based solely on a best fit to macroscopic adsorption data alone. The latter modeling approach may sometimes achieve an excellent fit to macroscopic adsorption data with fewer surface species (and model parameters), but the modeling approach developed in this study is superior because the surface species used (and their ranges of pH predominance) were supported by spectroscopic evidence. The modeling approach included an analysis of the dependence of calculated adsorption on the proton coefficients of surface reactions (combined with bond-valence analysis), and for one surface species, an analysis of surface charge distribution. Unfortunately, detection limits for the spectroscopic analysis at present only allow this modeling approach to be applied at relatively high adsorption densities. Extrapolation of the modeling results to lower adsorbate concentrations requires an analysis of surface site types and their likely abundances.

#### 4. Summary and conclusions

At  $p_{\text{CO}_2} = 10^{-3.45}$  atm, U(VI) uptake on imogolite surfaces was sensitive to changes in pH and ionic strength. The adsorption maximized at near neutral pH values, and decreased with increasing pH. An increase in sodium nitrate concentrations from 0.02 to 0.5 M resulted in decreasing U(VI) adsorption at pH > 7.5. Our comprehensive XAS analyses and PCA suggest: (1) U(VI) surface species are pH dependent and (2) mixed inner-sphere surface species and/or outer-sphere surface species are present within different pH regions.

As indicated by U–Al interatomic distances of  $\sim 3.3$  Å, inner-sphere surface species are coordinated on outer-wall  $\text{AlO}_6$  functional groups via bidentate mononuclear configuration. U–C interatomic distances of  $\sim 2.9$  Å were consistently observed at pH 5.3–8.8, suggesting bidentate bonding of carbonate anion on U(VI) equatorial oxygen atoms. Incorporation of U–O<sub>dist</sub> 3- and 4-legged multiple scattering paths as a function of U–O<sub>eq</sub>–C bending angle provided new insight into the complex U(VI)–carbonate ternary surface speciation at the imogolite–water interface. bis-Carbonato ternary and non-carbonato inner-sphere surface species co-exist in different proportions at pH values 5.3 and 7. We found that pronounced U–O<sub>dis</sub> features at  $\sim 4.23$  Å in FT spectra at pH 8.8 could be attributed to the formation of tris-carbonato outer-sphere surface species, with approximately 30% of adsorbed U(VI) present as bis-carbonato inner-sphere surface species.

The results indicate that U(VI)–carbonato ternary species on poorly crystalline aluminosilicate mineral surfaces may be important in controlling U(VI) mobility in low-temperature geochemical environments over a wide pH range ( $\sim 5$ – $9$ ), even at the partial pressure of carbon dioxide of ambient air ( $p_{\text{CO}_2} = 10^{-3.45}$  atm). Knowledge of the macro- and molecular-scale uranyl (U(VI)) partitioning with soil/sediment mineral components will be important in future predictions of U(VI) transport processes in the vadose zone and in aquifers.

## Acknowledgments

Portions of this research were carried out at the Stanford Synchrotron Radiation Laboratory, a national user facility operated by Stanford University on behalf of the U.S. Department of Energy, Office of Basic Energy Sciences. The SSRL Structural Molecular Biology Program is supported by the Department of Energy, Office of Biological and Environmental Research, and by the National Institutes of Health, National Center for Research Resources, Biomedical Technology Program. We thank D. Sverjensky, M. Villalobos, G. Curtis, and three anonymous reviewers for their valuable comments.

Associate editor: Dimitri A. Sverjensky

## References

- Allard, B., Olofsson, U., Torstenfelt, B., 1984. Environmental actinide chemistry. *Inorg. Chim. Acta* **94**, 205–221.
- Allard, T., Ildefonse, P., Beaucaire, C., Calas, G., 1999. Structural chemistry of uranium associated with Si, Al, Fe gels in a granitic uranium mine. *Chem. Geol.* **158**, 81–103.
- Ames, L.L., McGarrah, J.E., Walker, B.A., 1983. Sorption of trace constituents from aqueous solutions onto secondary minerals. I. Uranium. *Clay. Clay Miner.* **31** (5), 321–334.
- Bargar, J.R., Brown Jr., G.E., Parks, G.A., 1997. Surface complexation of Pb(II) at oxide–water interfaces: I. XAFS and bond-valence determination of mononuclear and polynuclear Pb(II) sorption products on aluminum oxides. *Geochim. Cosmochim. Acta* **61** (13), 2617–2637.
- Bargar, J.R., Reitmeier, R., Davis, J.A., 1999. Spectroscopic confirmation of uranium(VI)–carbonate adsorption complexes on hematite. *Environ. Sci. Technol.* **33** (14), 2481–2484.
- Bargar, J.R., Reitmeier, R., Lenhart, J.J., Davis, J.A., 2000. Characterization of U(VI)–carbonato ternary complexes on hematite: EXAFS and electrophoretic mobility measurements. *Geochim. Cosmochim. Acta* **64** (16), 2737–2749.
- Belokoneva, E.L., Mokeeva, V.I., Kuznetsov, L.M., 1979. Crystal-structure of synthetic soddyite,  $(\text{UO}_2)_2(\text{SiO}_4)(\text{H}_2\text{O})_2$ . *Dokl. Akad. Nauk. SSSR* **246**, 93–96.
- Bernhard, G., Geipel, G., Reich, T., Amayri, S., Nitsche, H., 2001. Uranyl(VI) carbonate complex formation: validation of the  $\text{Ca}_2\text{UO}_2(\text{CO}_3)_3(\text{aq})$  species. *Radiochim. Acta* **89**, 511–518.
- Borovec, Z., 1981. The adsorption of uranyl species by fine clay. *Chem. Geol.* **32**, 45–58.
- Brese, N.E., O'Keefe, M., 1991. Bond-valence parameters for solids. *Acta Crystallogr. B* **47**, 192–197.
- Burns, P.C., Ewing, R.C., Hawthorne, F.C., 1997. The crystal chemistry of hexavalent uranium: polyhedral geometries, bond-valence parameters, and polymerization of polyhedra. *Can. Mineral.* **35**, 1551–1570.
- Catalano, J.G., Brown, J., 2004. Analysis of uranyl-bearing phases by EXAFS spectroscopy: interferences, multiple scattering, accuracy of structural parameters, and spectral differences. *Am. Mineral.* **89**, 1004–1021.
- Catalano, J.G., Trainor, T.P., Eng, P.J., Waychunas, G.A., Brown, J., 2005. CTR diffraction and grazing incidence EXAFS study of U(VI) adsorption onto  $\alpha\text{-Al}_2\text{O}_3$  and  $\alpha\text{-Fe}_2\text{O}_3$  (1102) surfaces. *Geochim. Cosmochim. Acta* **69** (14), 3555–3572.
- Chisholm-Brause, C.J., Conradson, S.D., Buscher, C.T., Eller, P.G., Morris, D.E., 1994. Speciation of uranyl sorbed at multiple binding sites on montmorillonite. *Geochim. Cosmochim. Acta* **58** (17), 3625–3631.
- Chisholm-Brause, C.J., Berg, J.M., Little, K.M., Matzner, R.A., Morris, D.E., 2004. Uranyl sorption by smectites: spectroscopic assessment of thermodynamic modeling. *J. Colloid Interf. Sci.* **277**, 366–382.
- Clark, C.J., McBride, M.B., 1984. Cation and anion retention by natural and synthetic allophane and imogolite. *Clay. Clay Miner.* **32** (4), 291–299.
- Cradwick, P.D., Wada, K., Russell, J.D., Yoshinga, N., Masson, C.R., 1972. Imogolite, a hydrated aluminum silicate of tubular structure. *Nature* **240** (104), 187–189.
- Dahlgren, R.A., Walker, W.J., 1993. Aluminum release rates from selected spodosol Bs horizons: effect of pH and solid-phase aluminum pools. *Geochim. Cosmochim. Acta* **57**, 57–66.
- Davis, J.A., 2001. Surface complexation modeling of uranium(VI) adsorption on natural mineral assemblages. U.S. Nuclear Regulatory Commission. NUREG/CR-6708.
- Davis, J.A., Meece, D.E., Kohler, M., Curtis, G.P., 2004. Approaches to surface complexation modeling of uranium(VI) adsorption on aquifer sediments. *Geochim. Cosmochim. Acta* **68** (18), 3621–3641.
- Den Auwer, C., Drot, R., Simoni, E., Conradson, S.D., Gailhanou, M., Mustre de Leon, J., 2003. Grazing incidence XAFS spectroscopy of uranyl sorbed onto  $\text{TiO}_2$  rutile surfaces. *New J. Chem.* **27**, 648–655.
- Denaix, L., Lamy, I., Bottero, J.Y., 1999. Structure and affinity towards  $\text{Cd}^{2+}$ ,  $\text{Cu}^{2+}$ ,  $\text{Pb}^{2+}$  of synthetic colloidal amorphous aluminosilicates and their precursors. *Colloid Surfaces A* **158** (3), 315–325.
- Denecke, M.A., Rothe, J., Dardenne, K., Lindqvist-Reis, P., 2003. Grazing incidence (GI) XAFS measurements of Hf(IV) and U(VI) sorption onto mineral surfaces. *Phys. Chem. Chem. Phys.* **5**, 939–946.
- Dent, A.J., Ramsay, J.D.F., Swanton, S.W., 1992. An EXAFS study of uranyl ion in solution and sorbed onto silica and montmorillonite clay colloids. *J. Colloid Interf. Sci.* **150** (1), 45–60.
- Dodge, C.J., Francis, A.J., Gillow, J.B., Halada, G.P., Eng, C., Clayton, C.R., 2002. Association of uranium with iron oxides typically formed on corroding steel surfaces. *Environ. Sci. Technol.* **36**, 3504–3511.
- Duff, M.C., Amrhein, C., 1996. Uranium(VI) adsorption on goethite and soil in carbonate solutions. *Soil Sci. Soc. Am. J.* **60**, 1393–1400.

- Elzinga, E.J., Tait, C.D., Reeder, R.J., Rector, K.D., Donohoe, R.T., Morris, D.E., 2004. Spectroscopic investigation of U(VI) sorption at the calcite–water interface. *Geochim. Cosmochim. Acta* **68** (11), 2437–2448.
- Farmer, V.C., Adams, M.J., Fraser, A.R., Palmieri, F., 1983. Synthetic imogolite: properties, synthesis, and possible applications. *Clay Miner.* **18**, 459–472.
- Farmer, V.C., Fraser, A.R., 1982. Chemical and colloidal stability of soils in the  $\text{Al}_2\text{O}_3\text{--Fe}_2\text{O}_3\text{--SiO}_2\text{--H}_2\text{O}$  system: their role in podzolization. *J. Soil Sci.* **33**, 737–742.
- Fox, P.M., Davis, J.A., Zachara, J.M., 2006. The effect of calcium on aqueous uranium(VI) speciation and adsorption to ferrihydrite and quartz. *Geochim. Cosmochim. Acta* **70** (6), 1379–1387.
- Glinka, Y.D., Krak, T.B., Belyak, Y.N., Degoda, V.Y., Ogenko, V.M., 1995. X-ray and photo-luminophors based on  $\text{SiO}_2\text{--UO}_2^{2+}$  adsorption systems. *Colloid Surface A* **104**, 17–27.
- Goodman, B.A., Russell, J.D., Montez, B., Oldfield, E., Kirkpatrick, R.J., 1985. Structural studies of imogolite and allophanes by Al-27 and Si-29 nuclear magnetic-resonance spectroscopy. *Phys. Chem. Miner.* **12** (6), 342–346.
- Guillaumont, R., Fanghanel, T., Neck, V., Fuger, J., Palmer, D.A., Grenthe, I., Rand, M.H., 2003. *Update on the Chemical Thermodynamics of Uranium, Neptunium, Plutonium, Americium, and Technetium*. Elsevier, Amsterdam.
- Gustafsson, J.P., 2001. The surface chemistry of imogolite. *Clay. Clay Miner.* **49** (1), 73–80.
- Harsh, J., Chorover, J., Nizeyimana, E., 2002. Allophane and imogolite. In: Dixon, J.B., Schulze, D.G. (Eds.), *Soil Mineralogy with Environmental Applications*, vol. SSSA book series. Soil Science Society of America, pp. 291–322.
- Harsh, J.B., Traina, S.J., Botle, J., Yang, Y., 1992. Adsorption of cations on imogolite and their effect on surface-charge characteristics. *Clay. Clay Miner.* **40** (6), 700–706.
- Hennig, C., Reich, T., Dähn, R., Scheidegger, A.M., 2002. Structure of uranium sorption complexes at montmorillonite edge sites. *Radiochim. Acta* **90**, 653–657.
- Herbelin, A.L., Westall, J.C., 1999. FITEQL: A computer program for the determination of chemical equilibrium constants from experimental data, Version 4.0. Report 99-01. Chemistry Department, Oregon State University, Corvallis, Oregon.
- Hiemstra, T., Riemsdijk, W.H.V., Bolt, G.H., 1989. Multisite proton adsorption modeling at the solid/solution interface of (hydr)oxides: a new approach. I. Model description and evaluation of intrinsic reaction constants. *J. Colloid Interf. Sci.* **133**, 91–104.
- Ho, C.H., Miller, N.H., 1985. Effect of humic acid on uranium uptake by hematite particles. *J. Colloid Interf. Sci.* **10**, 281–288.
- Horikawa, Y., 1975. Electrokinetic phenomena of aqueous suspensions of allophane and imogolite. *Clay Sci.* **4** (255–263).
- Hoshino, H., Urakawa, H., Donkai, N., Kajiwar, K., 1996. Simulation of mesophase formation of rodlike molecule, imogolite. *Polym. Bull.* **36**, 257–264.
- Hsi, C.-K.D., Langmuir, D., 1985. Adsorption of uranyl onto ferric oxyhydroxides: application of the surface complexation site-binding model. *Geochim. Cosmochim. Acta* **49**, 1931–1941.
- Hudson, E.A., Allen, P.G., Terminello, L.J., Denecke, M.A., Reich, T., 1996. Polarized X-ray absorption spectroscopy of the uranyl ion: comparison of experiment and theory. *Phys. Rev. B* **54**, 156–165.
- Ildefonse, P., Kirkpatrick, R.J., Montez, B., Calas, G., Flank, A.M., Lagarde, P., 1994.  $^{27}\text{Al}$  mas NMR and aluminum X-ray absorption near edge structure study of imogolite and allophanes. *Clay. Clay Miner.* **42** (3), 276–287.
- Jongmans, A.G., Verburg, P., Nieuwenhuys, A., Oort, F.v., 1995. Allophane, imogolite, and gibbsite in coatings in a Costa Rican Andisol. *Geoderma* **64**, 327–342.
- Karube, J., Nakaishi, K., Sugimoto, H., Fujihira, M., 1992. Electrokinetics behavior of imogolite under alkaline conditions. *Clay. Clay Miner.* **40** (6), 625–628.
- Koretsky, C.M., Sverjensky, D.A., Sahai, N., 1998. A model of surface site types on oxide and silicate minerals based on crystal chemistry: implications for site types and densities, multi-site adsorption, surface infrared spectroscopy, and dissolution kinetics. *Am. J. Sci.* **298**, 349–438.
- Lieser, K.H., Quandt-Klenk, S., Thybusch, B., 1992. Sorption of uranyl ions on hydrous silicon dioxide. *Radiochim. Acta* **57**, 5455–5464.
- Malinowski, E.R., 1991. *Factor Analysis in Chemistry*. John Wiley, New York.
- Manceau, A., Charlet, L., Boisset, M.C., Didier, B., Spadini, L., 1992. Sorption and speciation of heavy metals on hydrous Fe and Mn oxides. From microscopic to macroscopic. *Appl. Clay Sci.* **7**, 201–223.
- Maya, L., 1982. Sorbed uranium(VI) species on hydrous titania, zirconia, and silica gel. *Radiochim. Acta* **31**, 147–151.
- McKeague, J.A., Kodama, H., 1981. Imogolite in cemented horizons of some British Columbia soils. *Geoderma* **25** (3–4), 189–197.
- McKinley, J.P., Zachara, J.M., Smith, S.C., Turner, G.D., 1995. The influence of uranyl hydrolysis and multiple site-binding reactions on adsorption of U(VI) to montmorillonite. *Clay. Clay Miner.* **43** (5), 586–598.
- Mereiter, K., 1986. Neue kristallographische daten ueber das uranmineral andersonit. New crystallographic data of the uranium mineral andersonite. *Anzeiger der Oesterreichischen Akademie der wissenschaften, mathematisch-naturwissenschaftliche Klasse* **123** (3), 39–41.
- Morris, D.E., Chisholm-Brause, C.J., Barr, M.E., Conradson, S.D., Eller, P.G., 1994. Optical spectroscopic studies of the sorption of  $\text{UO}_2^{2+}$  species on a reference smectite. *Geochim. Cosmochim. Acta* **58** (17), 3613–3623.
- Morrison, S.J., Spangler, R.R., Tripathi, V.S., 1995. Adsorption of uranium(VI) on amorphous ferric oxyhydroxide at high concentrations of dissolved carbon(IV) and sulfur(VI). *J. Contam. Hydrol.* **17**, 333–346.
- Moyes, L.N., Parkman, R.H., Charnock, J.M., Vaughan, D.J., Livens, F.R., Hughes, C.R., Braithwaite, A., 2000. Uranium uptake from aqueous solution by interaction with goethite, lepidocrocite, muscovite, and mackinawite: an X-ray absorption spectroscopy study. *Environ. Sci. Technol.* **34**, 1062–1068.
- Nakayama, F.S., 1971. Thermodynamic functions for the dissociation of  $\text{NaHCO}_3$ ,  $\text{NaCO}_3$ ,  $\text{HCO}_3^-$ , and  $\text{H}_2\text{CO}_3$ . *J. Inorg. Nucl. Chem.* **33**, 1287–1291.
- Parfitt, R.L., Russel, J.D., 1977. Adsorption on hydrous oxides IV. Mechanisms of adsorption of various ions goethite. *J. Soil Sci.* **28**, 297–305.
- Payne, T.E., Davis, J.A., Waite, T.D., 1998. Uranium(VI) adsorption on model minerals: controlling factors and surface complexation modeling. In: Jenne, E.A. (Ed.), *Adsorption of Metals by Geomedia*. Academic Press, New York, pp. 75–97.
- Payne, T.E., Edis, R., Fenton, B.R., Waite, T.D., 2001. Comparison of laboratory uranium sorption data with 'In situ distribution coefficients' at the Koongarra deposit, Northern Australia. *J. Environ. Radioactiv.* **57** (1), 35–55.
- Payne, T.E., Waite, T.D., 1991. Surface complexation modeling of uranium sorption data obtained by isotopic exchange techniques. *Radiochim. Acta* **52/53**, 487–493.
- Piasecki, W., 2002. 1pK and 2pK protonation models in the theoretical description of simple ion adsorption at the oxide/electrolyte interface: the analysis of temperature dependence of potentiometric titration curves. *J. Colloid Interf. Sci.* **254** (1), 56–63.
- Piret, P., Declercq, J.-P., Wauters-Stoop, D., 1979. Structure of phurallumite. *Acta Crystallogr. Sect. B* **35**, 1880–1882.
- Pohl, P.I., Faulon, J., Smith, D.M., 1996. Pore structure of imogolite computer models. *Langmuir* **12**, 4463–4468.
- Prikryl, J.D., 1994. Uranium sorption on  $\alpha$ -alumina: effects of pH and surface area/solution-volume ratio. *Radiochim. Acta* **66/67**, 291–296.
- Rehr, J.J., Albers, R.C., Zabinsky, S.I., 1992. High-order multiple scattering calculations of X-ray absorption fine structure. *Phys. Rev. Lett.* **69**, 3379–3400.
- Reich, T., Moll, H., Denecke, M.A., Geipel, G., Bernhard, G., Nitsche, H., Allen, P.G., Bucher, J.J., Kaltsoyannis, N., Edelstein, N.M., Shuh, G.



- D.K., 2003. Characterization of hydrous uranyl silicate by EXAFS. *Radiochim. Acta* **74**, 219–223.
- Riley, R.G., Zachara, J.M., Wobber, F.J., 1992. Chemical contaminant mixtures for subsurface science research on DOE lands and selection of contaminants. U.S. Department of Energy.
- Sverjensky, D.A., 2005. Prediction of surface charge on oxides in salt solutions: revisions for 1:1 (M+L-) electrolyte. *Geochim. Cosmochim. Acta* **69** (2), 225–257.
- Sylwester, E.R., Hudson, E.A., Allen, P.G., 2000. The structure of uranium (VI) sorption complexes on silica, alumina, and montmorillonite. *Geochim. Cosmochim. Acta* **64** (14), 2431–2438.
- Teo, B.K., 1986. *EXAFS: Basic Principles and Data Analysis*. Springer-Verlag, Berlin.
- Theng, B.K.G., Russell, M., Churchman, G.J., Parfitt, R.L., 1982. Surface properties of allophane, halloysite, and imogolite. *Clay. Clay Miner.* **30**, 143–149.
- Violante, P., Tait, J.M., 1979. Identification of imogolite in some volcanic soils from Italy. *Clay Miner.* **14** (2), 155–158.
- Wada, S., 1987. Adsorption of Al(III) on allophane, imogolite, goethite, and noncrystalline silica and the extractability of the adsorbed Al(III) in 1 M KCl solution. *Soil Sci. Plant Nutr.* **33** (3), 487–491.
- Wada, S., Eto, A., Wada, K., 1979. Synthetic allophane and imogolite. *J. Soil Sci.* **30**, 347–355.
- Waite, T.D., Davis, J.A., Payne, T.E., Waychunas, G.A., Xu, N., 1994. Uranium(VI) adsorption to ferrihydrite: application of a surface complexation model. *Geochim. Cosmochim. Acta* **58** (24), 5465–5478.
- Walter, M., Arnold, T., Reich, T., Bernhard, G., 2003. Sorption of uranium(VI) onto ferric oxides in sulfate-rich acid waters. *Environ. Sci. Technol.* **37**, 2898–2904.
- Webb, S.M., 2005. A graphical user interface for XAS analysis using IFEFFIT. *Phys. Scr. (T115)*, 1011–1014.